Wall vortex induced by the collapse of a near-wall cavitation bubble: Influence of the water surface

Jianlin Huang
Key Laboratory for Mechanics in Fluid Solid Coupling Systems, Institute of Mechanics, Chinese Academy of Sciences, Beijing 100190, People's Republic of China and School of Future Technology, University of Chinese Academy of Sciences, Beijing 100049, People's Republic of China

Jingzhu Wang*
Key Laboratory for Mechanics in Fluid Solid Coupling Systems, Institute of Mechanics, Chinese Academy of Sciences, Beijing 100190, People's Republic of China; School of Engineering Science, University of Chinese Academy of Sciences, Beijing 100049, People's Republic of China; and Guangdong Aerospace Research Academy, Guangzhou 511458, People's Republic of China

Wenlu Guo
School of Aeronautics and Astronautics, Zhejiang University, Zhejiang 310027, People's Republic of China

Yiwei Wang†
Key Laboratory for Mechanics in Fluid Solid Coupling Systems, Institute of Mechanics, Chinese Academy of Sciences, Beijing 100190, People's Republic of China; School of Future Technology, University of Chinese Academy of Sciences, Beijing 100049, People's Republic of China; and School of Engineering Science, University of Chinese Academy of Sciences, Beijing 100049, People's Republic of China

(Received 4 February 2024; accepted 23 April 2024; published 8 May 2024)

Wall vortex occurs when a cavitation bubble oscillates far from a single rigid wall (at a dimensionless standoff distance of $\gamma_r > 1.3$). This study reveals that introducing a water surface expands the wall vortex regime. A wall vortex in an expanded new regime forms instead of a free vortex at a smaller γ_r value. Because of the influence of the water surface, a broader jet pierces the bottom of a bubble. This causes the bubbles to expand easily along the wall and form a flat shape during the second cycle. Here an outwards flow forms instead of an upward flow after the bubble recollapses. This study investigates the formation and development of a wall vortex in the new expanded regime via a combination of experiments, numerical simulations, and theoretical modeling. To this end, a theoretical model describing the radial motion R and centroid position h of the bubble between the boundaries is developed using Lagrangian formulation. Two infinite sets of image bubbles are used to satisfy the conditions of the water surface and rigid wall based on image theory. The criteria for the vortex flow patterns are proposed based on the direction of the centroid migration $\dot{h}(t_c)$ of the bubble at the beginning of the second cycle t_c. A free vortex occurs when the upward flow dominates [$\dot{h}(t_c) > 0$], whereas a downwards flow dominates the

*Corresponding author: wangjingzhu@imech.ac.cn
†Corresponding author: wangyw@imech.ac.cn

wall vortex [$\dot{h}(t_c) < 0$]. A phase diagram of the vortex flows is obtained from the theoretical model and is verified using the experimental results. Numerical analysis reveals that the wall vortex flow with the influence of the water surface contributes to a greater wall shear stress and larger area, thereby increasing the potential for surface cleaning. These findings provide new insights for engineering applications such as ultrasonic cleaning.

DOI: 10.1103/PhysRevFluids.9.053602

I. INTRODUCTION

Bubble dynamics near a rigid wall were first studied to understand the erosion mechanism attributable to hydrodynamic cavitation [1,2]. The key issue in this context is the toroidal collapse resulting from a re-entrant jet, which further induces unsteady flow fields. Two vortex flow patterns were observed based on the nondimensional standoff distance γ_r of the bubble to the rigid wall: (i) a free vortex that migrates away from the rigid wall and (ii) a wall vortex that spreads along the wall [3]. Vortex flows exhibit impressive shear, thereby resulting in considerable wall-normal forces and large shear stresses on the wall [4–6], which can be exploited for applications such as ultrasonic cleaning, sonoporation, drug delivery, and laser surgery [7–10].

Kornfeld and Suvorov [11] first suggested that a bubble might collapse asymmetrically and produce a jet pointing towards a nearby rigid wall. The asymmetry of the collapse results from the pressure gradient [12]. Further, bubble dynamics near the rigid walls have been widely studied using experiments, numerical simulations, and theoretical modeling [13–25]. Brujan *et al.* [26] conducted numerical simulations to investigate the velocity and pressure fields in a liquid surrounding a bubble. They found that a ring vortex formed after the jet impacted a rigid wall and later spread along the wall. Reuter *et al.* [3] investigated vortex flows after a laser-induced bubble collapse using a hybrid particle image and tracking velocimetry technique. They summarized the flow field patterns as functions of γ_w, such as the wall and free vortex, after multiple oscillations. Saini *et al.* [27] conducted direct numerical simulations to study the formation of the vortex flows. An annular jet formed parallel to the wall, thereby resulting in flows directed upward and a free vortex. Wall vortex and free vortex patterns were observed in the collapse of a cavitation bubble near a sand bed in a study conducted Sieber *et al.* [28]. Huang *et al.* [29] presented the formation of two vortex flow patterns induced by the collapse of a cavitation bubble near a rigid wall: [Fig. 1(a)] a free vortex migrating away from the wall and [Fig. 1(b)] a wall vortex spreading along the wall. They discussed the influence of wall wettability on the vortex flow, and suggested that the main area of the shear stress be enlarged spatially and temporally in the case of superhydrophobic surfaces. The aforementioned studies demonstrated that the formation and development of a vortex flow are determined principally by the behavior of the bubble near the boundary.

The behavior of the bubbles varies considerably when they are initiated between different boundaries such as two perpendicular rigid walls [30], two parallel rigid walls [31], or a rigid wall and an elastic boundary [1]. With the development of the laser-induced forward transfer technique, bubble dynamics between a rigid wall and water surface have received increased attention [32]. Gregorcic *et al.* [33] presented experimental measurements of a cavitation bubble oscillating between a free surface and rigid wall using the deflections of a laser beam as the optical probe. They found that the collapse time of the bubbles was shortened and prolonged by the water surface and rigid wall boundary, respectively. Zhang *et al.* [34] argued that most of the motion features observed in the double-boundary cases originate from the single-boundary cases, in addition to changes in the speed and height. Huang *et al.* [35] experimentally observed three distinct patterns identified from the morphologies of the bubbles and water surfaces. The dynamic characteristics of the bubbles in the collapse and rebound stages varied between the different patterns. Lui *et al.* [36] performed qualitative analyses of the behavior of the bubbles and water surfaces based on two-dimensional standoff distances. The above-mentioned studies focused on analyzing the characteristics of the

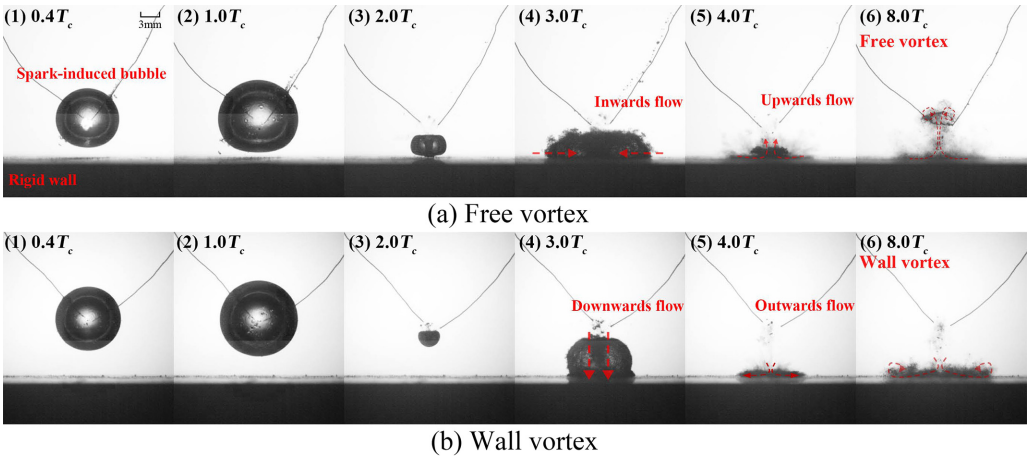

FIG. 1. Formation of two patterns of the vortex flows induced by the collapse of the cavitation bubbles near a single rigid wall: (a) free vortex at $\gamma_r = 1$ and (b) wall vortex at $\gamma_r = 1.5$. The red arrows represent the directions of the flow. The values of T_c are 11.94 ms at $\gamma_r = 1$ and 12.08 ms at $\gamma_r = 1.5$, respectively.

bubble and water surface, such as the velocity of the jet and height of the water skirt. Currently, the vortex flow induced by the oscillations of the cavitation bubbles between the boundaries is not fully understood. Additionally, applications, such as ultrasonic cleaning and sonoporation, are performed at different boundaries. Hence, it is necessary to understand the characteristics of the vortex flow patterns between different boundaries to determine appropriate applications.

This study provides insights into the formation and development of vortex flows induced by a cavitation bubble between a water surface and rigid wall. A combination of experiments, numerical simulations, and theoretical modeling was used. This paper is divided as follows: Section II describes the methodologies used in the experiments, theoretical modeling, and numerical simulations. In Sec. III A, the influence of the water surface on the vortex flow patterns is presented through experimental observations. The mechanisms of the bubble collapse and the subsequently generated vortex flow under the influence of the water surface are discussed numerically in Sec. III B. Section III C presents the criteria for the different vortex flow patterns and the corresponding phase diagram obtained from the theoretical model. Finally, Sec. IV summarizes the study.

II. METHODOLOGIES

A. Experimental setup

As shown in Fig. 2, an experiment was conducted to observe the collapse and subsequent vortex flow induced by a spark-induced bubble between a rigid wall and water surface. On discharge, the strong Joule heating at the crossing point of the two electrodes vaporizes the surrounding water, thereby generating a centimeter-scale cavitation bubble, as reported in previous studies [37,38]. This crossing point was the initial center of the bubble. The voltage was set to 240 V, while the electrodes were a pair of 0.3-mm-diameter copper wires. To eliminate the effect of the discharge spark on the initial expansion of the bubble, a pulsed laser (Cavilux HF810, 810-nm wavelength and 500-W output) with a filter was used as the light source. The laser light and high-speed camera (V1612, Phantom Co., Ltd., USA) were operated simultaneously when the electric discharge was triggered. The sampling frequency of the high-speed camera was 73 kfps, exposure time was 2 μs, and image resolution was 7 px/mm.

As shown in Fig. 2(b), the two-dimensional standoff distances are defined as $\gamma_w = h_w/R_{\max}$ and $\gamma_r = h_r/R_{\max}$, wherein h_w is the distance from the initial center of the bubble to the water surface,

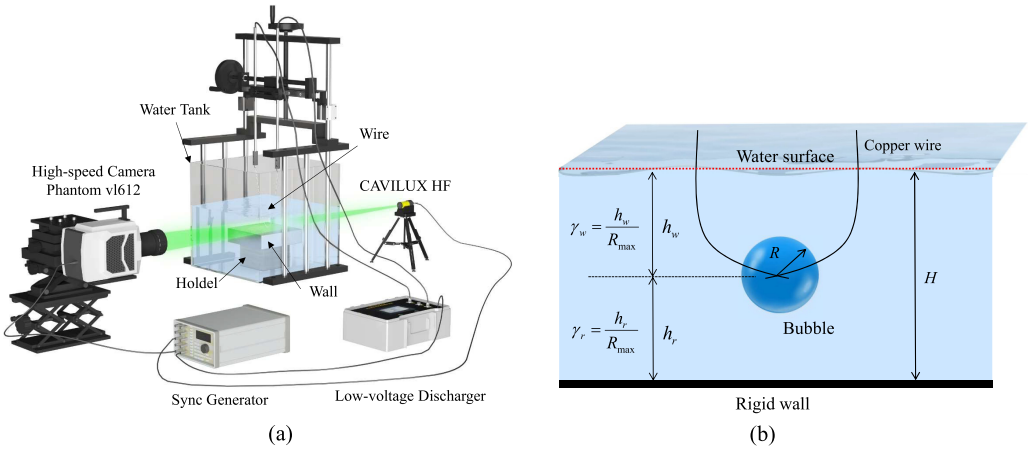

FIG. 2. Schematic of the experimental setup for observing the behaviors of a spark-induced bubble between a rigid wall and water surface: (a) Experimental setup and (b) definitions of the two nondimensional stand-off distances (γ_r to the rigid wall and γ_w to the water surface). In (a), the green path represents the light source originating from the pulsed laser.

h_r the distance to the rigid wall, and $R_{\max}$ the maximum bubble radius [16]; h_w and h_r were varied by adjusting the positions of the crossing points of the copper wires and water surface. A value of $R_{\max} = 12 \pm 0.14$ mm was obtained after repeated experiments in an unbounded liquid. The bubble equivalent radius and centroid position were calculated from the gray values in the image using the Open Computer Vision Library (OpenCV) [39]. More details are shown in Appendix A.

B. Theoretical model

This section presents a theoretical model for describing the radial motion and centroid migration of a cavitation bubble between boundaries using a Lagrangian formulation. Fluid mechanics is used to model an inviscid and incompressible fluid wherein the motion is irrotational. To solve the kinetic energy equations in the Lagrangian formulation, the image theory developed by Best [40,41] was used to obtain expressions for the velocity potential. As shown in Fig. 3, two infinite sets of image bubbles are used to satisfy the boundary conditions of a rigid wall of the water surface, that is, the zero normal velocity condition at the rigid wall and linearized boundary condition of a vanishing potential at the water surface [42]. The Lagrangian equation is expressed as follows:

$$L(\boldsymbol{x}, \dot{\boldsymbol{x}}, t) = K(\boldsymbol{x}, \dot{\boldsymbol{x}}, t) - E(\boldsymbol{r}), \tag{1}$$

where $\boldsymbol{x}$ and $\dot{\boldsymbol{x}}$ denote the sets of generalized coordinates and generalized velocities of the system, respectively, and K and E are the kinetic energy and potential energy of the system, respectively.

When the flow fields around multiple bubbles are described by a velocity potential ϕ that satisfies the Laplace equation, the kinetic energy K and potential energy V are expressed as follows:

$$K = -\frac{\rho}{2} \sum \int_{S_i} \phi(\dot{R}_i + \boldsymbol{U}_i \cdot \boldsymbol{n}_i) dS_i, \tag{2}$$

$$dV = \sum_i (P_\infty - P_i) dV_i = 4\pi \sum_i (P_\infty - P_i) R_i^2 dR_i, \tag{3}$$

where ρ is the density, ϕ the velocity potential, R_i the radius of the ith bubble, $\boldsymbol{U_i}$ the migration velocity of the centroid of the ith bubble, $\boldsymbol{n_i} = \boldsymbol{r}_i/|\boldsymbol{r}_i|$ the unit vector in the direction of $\boldsymbol{r_i}$, S_i the surface of the ith bubble, P_∞ the atmospheric pressure, and P_i the pressure on the surface of the

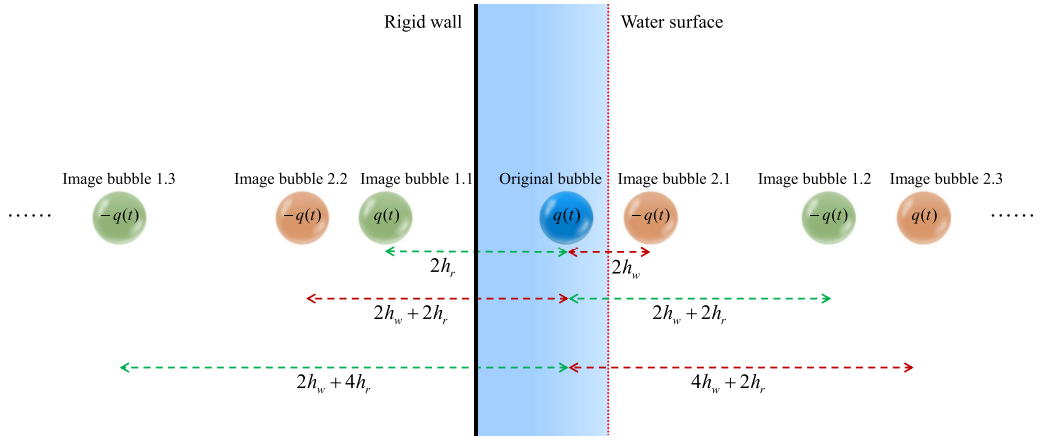

FIG. 3. Imaging system for the motion of a bubble between a water surface and rigid wall. To satisfy the boundary conditions, two infinite sets of image bubbles are used to represent the lowest-order contribution to the potential. The blue bubble represents the original bubble as a source of $q(t)$, the green and orange image bubbles the two infinite sets of image bubbles, $q(t)$ the image sources, and $-q(t)$ the image sinks.

liquid side of the ith bubble, which expressed as follows:

$$P_i = P_v + \left(P_\infty + \frac{2\sigma}{R_{i,\text{initial}}}\right)\left(\frac{R_{i,\text{initial}}}{R_i}\right)^{3\kappa} - \frac{2\sigma}{R_i}, \tag{4}$$

where P_v denotes the vapor pressure, $R_{i,\text{initial}}$ the initial radius of the ith bubble, κ the specific heat ratio, and σ the surface tension.

In the imaging system, two infinite sets of images are used to represent the lowest order contribution to the potential to satisfy the boundary conditions. The image bubbles reflected from the rigid wall had a similar source as the original bubbles, whereas those reflected from the water surface had the opposite influence. The positive and negative image bubbles are denoted as $q(t)$ and $-q(t)$, respectively.

Based on the study conducted by Ilinskii *et al.* [43], the velocity potential of the ith bubble surface was derived as expressed in Eq. (5), when the velocity potential of the system satisfies the Laplace equation and boundary conditions of the bubbles,

$$\phi\,|_{S_i} = -\left(R_i\dot{R}_i + \frac{R_i}{2}\boldsymbol{U}_i\cdot\boldsymbol{n}_i\right) + \sum_{m,m\neq i}\left\{-\left(\frac{R_m^2}{r_{im}}\dot{R}_m + \frac{R_m^3}{2r_{im}^2}\boldsymbol{U}_m\cdot\boldsymbol{n}_{mi}\right) + \frac{3R_iR_m^2}{2r_{im}^2}\dot{R}_m(\boldsymbol{n}_{mi}\cdot\boldsymbol{n}_i)\right.$$

$$\left. - \frac{3R_iR_m^3}{4r_{im}^3}[\boldsymbol{U}_m\cdot\boldsymbol{n}_i - 3(\boldsymbol{U}_m\cdot\boldsymbol{n}_{mi})(\boldsymbol{n}_{mi}\cdot\boldsymbol{n}_i)]\right\} + \sum_{j,m,m\neq i,j}\frac{R_j^2R_m^2}{2r_{im}^2r_{jm}^2}\cdot R_j(\boldsymbol{n}_{jm}\cdot\boldsymbol{n}_{mi}), \tag{5}$$

where r is the distance between the centers of the two bubbles.

Equations (6)–(8) provide the boundary conditions for the original bubble (R_0), positive image bubble (R_p), and negative image bubble (R_n),

$$\frac{\partial\phi}{\partial r_0} = \dot{R}_0 + \boldsymbol{U}_0\cdot\boldsymbol{n}_0, \quad \text{at } r_0 = R_0, \tag{6}$$

$$\frac{\partial\phi}{\partial r_p} = \dot{R}_p + \boldsymbol{U}_p\cdot\boldsymbol{n}_p, \quad \text{at } r_p = R_p, \tag{7}$$

$$\frac{\partial\phi}{\partial r_n} = -\dot{R}_n + \boldsymbol{U}_n\cdot\boldsymbol{n}_n, \quad \text{at } r_n = R_n. \tag{8}$$

Consequently, the kinetic energy K in the system is represented as follows when the velocity potential is preserved to the second order:

$$K = 2\pi\rho\left\{R_0^3\dot{R}_0^2 + \frac{1}{6}R_0^3U_0^2 + 2R_0^4\dot{R}^2\sum_{k=0}(-1)^k(\mathcal{A}_k - \mathcal{B}_k) + R_0^5\dot{R}(\boldsymbol{U}_0\cdot\boldsymbol{n}_{0k})\sum_{k=0}(-1)^k\left(\mathcal{A}_k^2 + \mathcal{B}_k^2\right)\right\}, \tag{9}$$

where

$$\mathcal{A}_k = \frac{1}{2}\frac{1}{(k+1)(h_r+h_w)-h_w}, \tag{10}$$

$$\mathcal{B}_k = \frac{1}{2}\frac{1}{k(h_r+h_w)+h_w}. \tag{11}$$

The Lagrang equations that describe a multibubble system are expressed as follows:

$$\frac{d}{dt}\left(\frac{\partial L}{\partial\dot{R}}\right) = \frac{\partial L}{\partial R}, \tag{12}$$

$$\frac{d}{dt}\left(\frac{\partial L}{\partial\dot{\boldsymbol{r}}}\right) = \frac{\partial L}{\partial\boldsymbol{r}}. \tag{13}$$

The equations for the radial motion $\ddot{R}$ and translational motion $\ddot{h}$ of the bubble were obtained by substituting the kinetic and potential energies into Eqs. (12) and (13) and are expressed as follows:

$$\ddot{R} = \frac{\frac{P-P_\infty}{\rho} + \frac{1}{4}U^2 - \frac{3}{2}\dot{R}^2\left[1 + \frac{4R}{3}\sum_{k=0}(-1)^k(\mathcal{A}_k - \mathcal{B}_k)\right]}{\left[R + R^2\sum_{k=0}(-1)^k(\mathcal{A}_k - \mathcal{B}_k)\right]}, \tag{14}$$

$$\ddot{h} = \dot{U} = -\frac{3\dot{R}U}{R} + \frac{9R\dot{R}^2 + 3R^2\ddot{R}}{4}\sum_{k=0}(-1)^k\left(\mathcal{A}_k^2 + \mathcal{B}_k^2\right), \tag{15}$$

where R and $\dot{R}$ are the radius and surface velocity of the bubble, respectively, and h and $\dot{h}$ the centroid position and migration velocity, respectively. Interested readers can refer to Appendix B for the detailed derivation.

Equations (10)—(11) suggest that the alternating series $\sum_{k=0}(-1)^k(\mathcal{A}_k - \mathcal{B}_k)$ and $\sum_{k=0}(-1)^k(\mathcal{A}_k^2 + \mathcal{B}_k^2)$ are absolutely convergent. Hence, it is reasonable to replace the sum of the infinite terms with that of the finite terms. The convergence and truncation errors are analyzed in Appendix D. The results showed that 13 image bubbles ($k = 3$) of the finite sets were considered to approximate the infinite sets in this study. The theoretical model was verified by comparing the radial motion and centroid migration to the experimental observations, as shown in Appendix D.

C. Numerical simulation

A numerical simulation was conducted using the multiphase compressible InterFoam solver in OpenFOAM. The pressure-based implicit splitting of operators (PISO) algorithm was used to solve transient compressible Navier-Stokes equations directly. The volume of fluid method was used to capture the gas–liquid interface. In the simulations, the gas and liquid phases were treated as compressible and immiscible Newtonian fluids without thermal effects or mass transfer [5,44,45].

The continuity and momentum equations are expressed as follows:

$$\frac{\partial \rho}{\partial t} + \nabla \cdot (\rho \boldsymbol{U}) = 0, \tag{16}$$

$$\frac{\partial \rho \boldsymbol{U}}{\partial t} + \nabla \cdot (\rho \boldsymbol{U}\boldsymbol{U}) = -\nabla p + \nabla \cdot \boldsymbol{\tau} + \sigma \kappa \nabla \alpha, \tag{17}$$

where ρ is the density, t the time, ∇ the gradient operator, $\boldsymbol{U}$ the velocity vector, p the pressure, $\boldsymbol{\tau}$ the viscous stress tensor, $\sigma = 0.07\,\mathrm{N\,m^{-1}}$ the surface tension coefficient, $\kappa = 1.4$ the specific heat ratio, and α the volume fraction.

The following adiabatic equation of state was used for the gas phase as expressed as follows [46]:

$$\rho = \rho_{g0}\left(\frac{p}{p_{g0}}\right)^{1/\kappa}, \tag{18}$$

where $p_{g0} = 10^5$ Pa is the reference pressure and $\rho_{g0} = 1.29\,\mathrm{kg\,m^{-3}}$ the gas-phase density at p_{g0}.

The Tait equation was used for the liquid phase as expressed as follows [6]:

$$\rho = \rho_{l0}\left(\frac{p + B}{p_{g0} + B}\right)^{1/\Gamma}, \tag{19}$$

where $\rho_{l0} = 1000\,\mathrm{kg\,m^{-3}}$ denotes the density of the liquid phase at p_{g0}, $\Gamma = 7.15$ the Tait exponent, and $B = 3.046 \times 10^8$ the Tait pressure.

The gas-liquid interface was obtained by solving the following transport equation for the phase volume fraction as expressed as follows [47]:

$$\frac{\partial \alpha}{\partial t} + \boldsymbol{U} \cdot \nabla \alpha + \nabla \cdot [\alpha(1-\alpha)\boldsymbol{U}_r] = -\alpha(1-\alpha)\left(\frac{1}{\rho_l}\frac{D\rho_l}{Dt} - \frac{1}{\rho_g}\frac{D\rho_g}{Dt}\right), \tag{20}$$

where $\boldsymbol{U_r}$ is the relative velocity between the two phases, also defined as $\boldsymbol{U}_r = c|\boldsymbol{U}|(\nabla\alpha/|\nabla\alpha|)$, c the artificial compression coefficient, ρ_l the liquid density, and ρ_g the gas density.

In summary, the governing equations are solved using the following steps: The phase-volume fraction equation is first solved, followed by the continuity and momentum equations. The equation of state was then used to update the density of each phase, while a pressure correction was initiated. Once the desired solution accuracy was achieved, the pressure correction and PISO cycle were terminated. This procedure is repeated with each step until the scheduled solution time os is reached.

Figure 4 shows a schematic of the computational modeling process. In the simulations, an axisymmetric model with a one-degree wedge structure was used in the computational domain. The calculation domain was set to 240 mm in width and 240 mm in height. As shown in Fig. 4(b), the wedge boundary conditions were imposed on the front and back planes of the wedge structure. The right boundary is an axis of symmetry, both the upper and left boundaries correspond with the outlet conditions, and the lower boundary is a rigid wall. A structural grid was used for all the computational domains, and the grid around the bubble was further refined to a minimum spacing of $\Delta x = 60$ μm to ensure an accurate capture of the interface and flow details. The total number of grid cells is 580 000. According to previous studies [5], the complex physics of the bubble nucleation begins with a spherical gas bubble with a high internal pressure. The initial bubble radius and internal pressure were set when the maximum sizes and collapse times of the bubbles in the simulation corresponded with the experimental observations. The maximum sizes of the bubbles $R_{\max}$ are 12.06 and 12.21 mm at $\gamma_r = 1.5$ and $\gamma_w = 2.5$ in the experiment and simulation, respectively, while they are 11.97 and 12.20 mm at $\gamma_r = 2$ and $\gamma_w = 3$, respectively. An analysis of the grid independence was performed, as shown in Appendix C. This analysis shows that the grid resolution used in this study is sufficient to describe the bubble behavior and flow fields around the bubble.

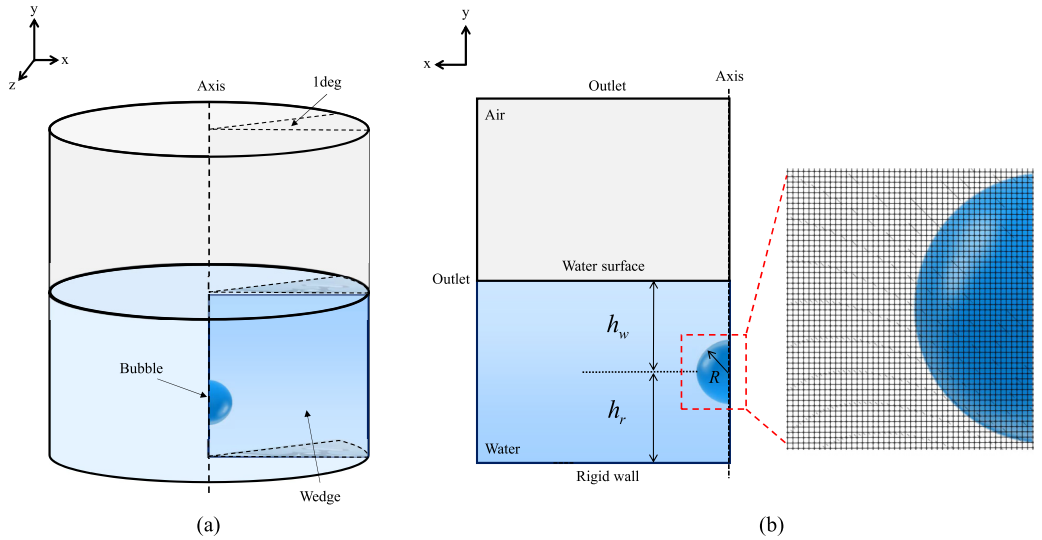

FIG. 4. Schematic of the computational modeling process: (a) Computational domain and (b) boundary condition settings. In (b), the size of the calculation domain is set to 240 mm in width and 240 mm in height.

III. RESULTS AND DISCUSSIONS

A. Influence of water surface on vortex flow

When a bubble collapses near a single rigid wall, two distinctive vortex flow patterns are observed after the second cycle as γ_r decreases: (i) a wall vortex spreads along the wall and (ii) a free vortex migrates away from the wall [3]. Compared to a single rigid wall, we discovered that a wall vortex was generated instead of a free vortex at a smaller γ_r value when introducing a water surface. A new wall vortex regime was induced owing to the influence of the water surface. In this section, we experimentally analyze the formation of the wall vortex in the newly expanded regime. In addition, the variables are nondimensionalized with the time when bubble reaches the maximum size T_c and the maximum radius of the bubble $R_{\max}$.

A free vortex forms after the oscillations of a spark-induced bubble at $\gamma_r = 1$ without the influence of the water surface (see Fig. 1). When a bubble is generated between the rigid wall and water surface, the vortex flow pattern does not change owing to the small influence of the water surface at $\gamma_r = 1$ and $\gamma_w = 2$. As shown in Fig. 5, the spark-induced bubble expanded and reached its first maximum radius at $1.0T_c$ after the electrical discharge was triggered. As the bubble shrinks, its bottom surface deforms into a semielliptical shape, while the upper surface quickly moves down. At $1.8T_c$, a jet generated from the top of the bubble pierced the bottom, while the bubble broke into two toroidal bubbles at $2.02T_c$. After the jet impacted the wall, the lower main bubble rebounded at $2.2T_c$ and reached its second maximum at $3.0T_c$. Further, the bubble surface contracted in the direction parallel to the wall more rapidly than that perpendicular to the wall. After the recollapse, the bubble migrates upward at $3.9T_c$. This indicates that the inward flow parallel to the wall dominated and converged to the axis of symmetry, thereby resulting in an upward flow directed away from the wall. Finally, a free vortex forms, thereby trapping the remaining bubbles and causing them to migrate upward at $5.3T_c$.

As γ_w further decreases, a wall vortex is formed instead of a free vortex, as shown in Fig. 6. As the bubbles expanded, the water surface moved upwards, thereby forming a liquid column. During shrinkage, a jet is induced, thereby pointing away from the water surface and towards the rigid wall. The width of the jet was broader than that shown in Fig. 5. After the broader jet penetrates the bottom, the bubbles expand along the wall and form a flat shape at $3.8T_c$. As the bubble recollpases,

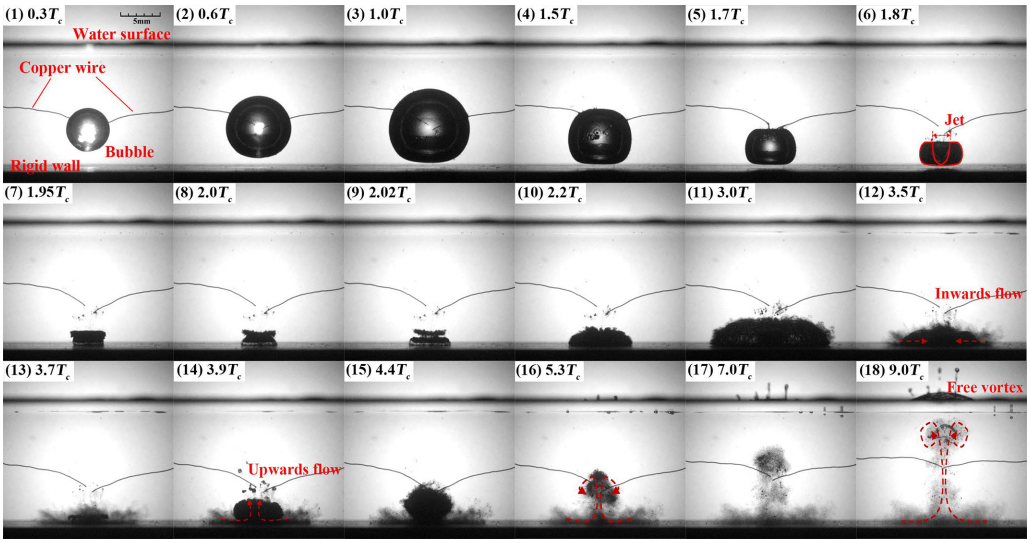

FIG. 5. Formation of a free vortex at $\gamma_r = 1$ and $\gamma_w = 2$: [(1)–(8)] the first cycle, [(9)–(13)] the second cycle, and [(14)–(20)] the subsequent oscillations of the bubble and migration of the generated free vortex. In this case, experiment $R_{\max} = 11.97$ mm and $T_c = 1.10$ ms. The flow induced by the bubble collapse is obtained from the image sequences of the experimental observations and the red arrows represent the directions of the flow. An animation of this case is available in video [48].

the upper surface of the flat-shaped bubble simultaneously impacts the wall at $4.0T_c$. Further, the bubble migrates along the wall at $5.0T_c$. This indicated that an outwards flow along the wall was induced instead of an upward flow. A wall vortex was observed owing to the migration of the remnant bubble at $5.0T_c$.

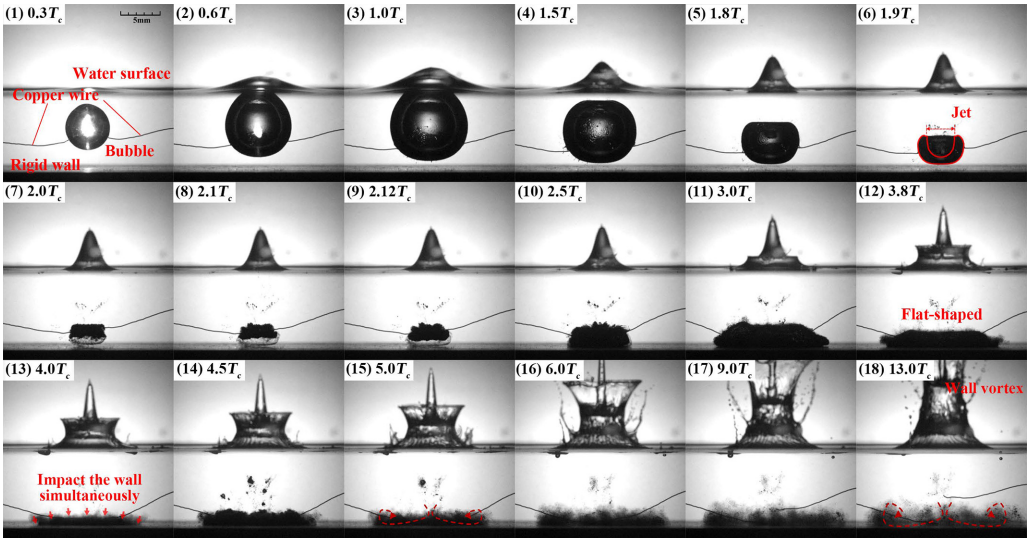

FIG. 6. Formation of a wall vortex at $\gamma_r = 1$ and $\gamma_w = 1$: [(1)–(8)] the first cycle, [(9)–(13)] the second cycle, and [(14)–(20)] the subsequent oscillations of the bubble and migration of the generated wall vortex. In this case, experiment $R_{\max} = 11.97$ mm and $T_c = 1.10$ ms. The flow induced by the bubble collapse is obtained from the image sequences of the experimental observations, while the red arrows represent the directions of the flow. An animation of this case is available in video [48].

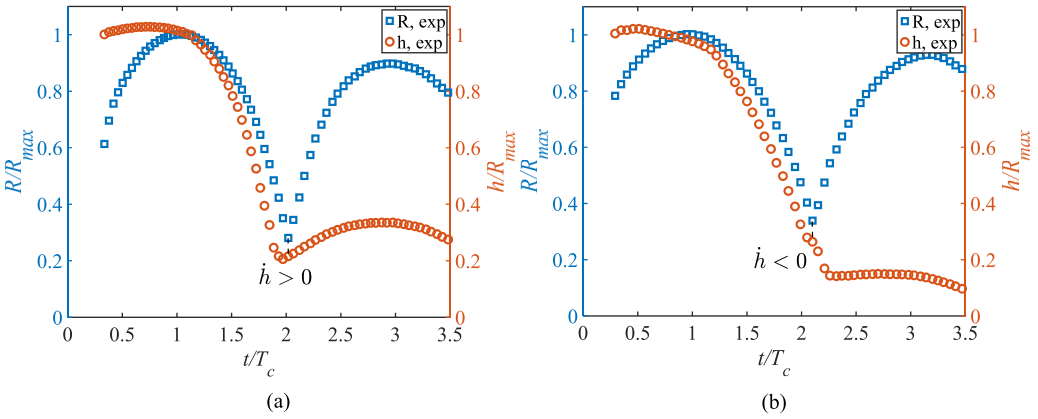

FIG. 7. Experimental results for the equivalent radius R and centroid position h of a spark-induced bubble: (a) free vortex at $\gamma_r = 1$ and $\gamma_w = 2$ and (b) wall vortex at $\gamma_r = 1$ and $\gamma_w = 1$. The blue squares and orange circles represent the equivalent radius and centroid position, respectively.

We obtained the bubble equivalent radii and centroid positions using OpenCV [39] from the experimental observations presented in Figs. 5 and 6. In Fig. 7, the abscissa represents the time, whereas the ordinates on the left and right represent the bubble radius and centroid position, respectively. A value of zero for the ordinates indicates the position of the rigid wall. In these two cases, the centroid position h hardly migrated during the expansion of the first cycle. The bubbles were accelerated to migrate downwards owing to the nonspherical collapse and downwards

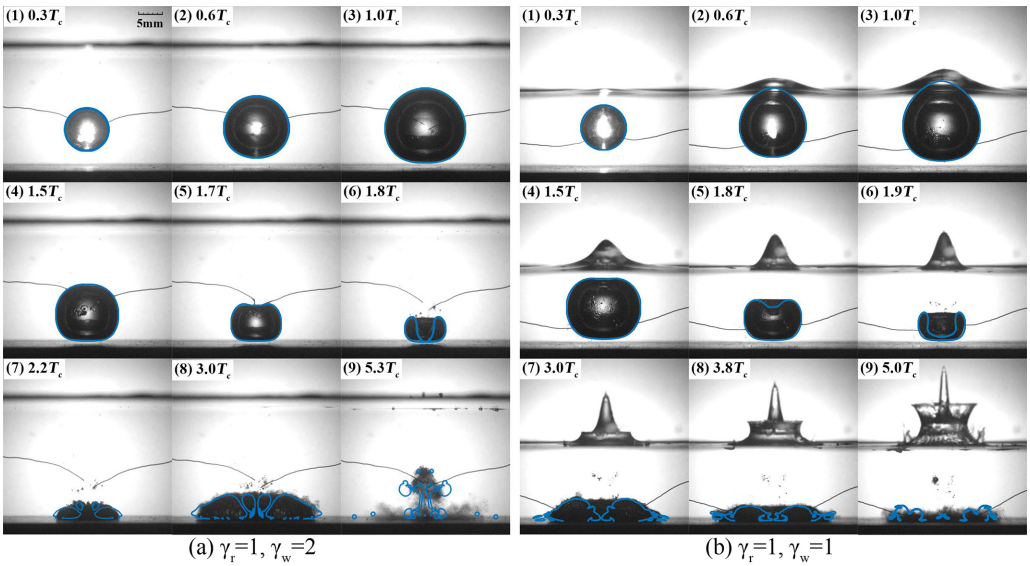

FIG. 8. Comparisons of the bubble shape evolution between experimental observations and numerical simulations. (a) Free vortex at $\gamma_r = 1$ and $\gamma_w = 2$: Experiment $R_{\max} = 12.06$ mm, $T_c = 1.31$ ms; simulation $R_{\max} = 12.21$ mm, $T_c = 1.32$ ms. (b) Wall vortex at $\gamma_r = 1$ and $\gamma_w = 1$: Experiment $R_{\max} = 11.97$ mm, $T_c = 1.10$ ms; simulation $R_{\max} = 12.20$ mm, $T_c = 1.12$ ms. The experimental observations are shown in the background, and the numerical simulations as blue contours. The contours represent the bubble shape at a volume fraction of 0.5.

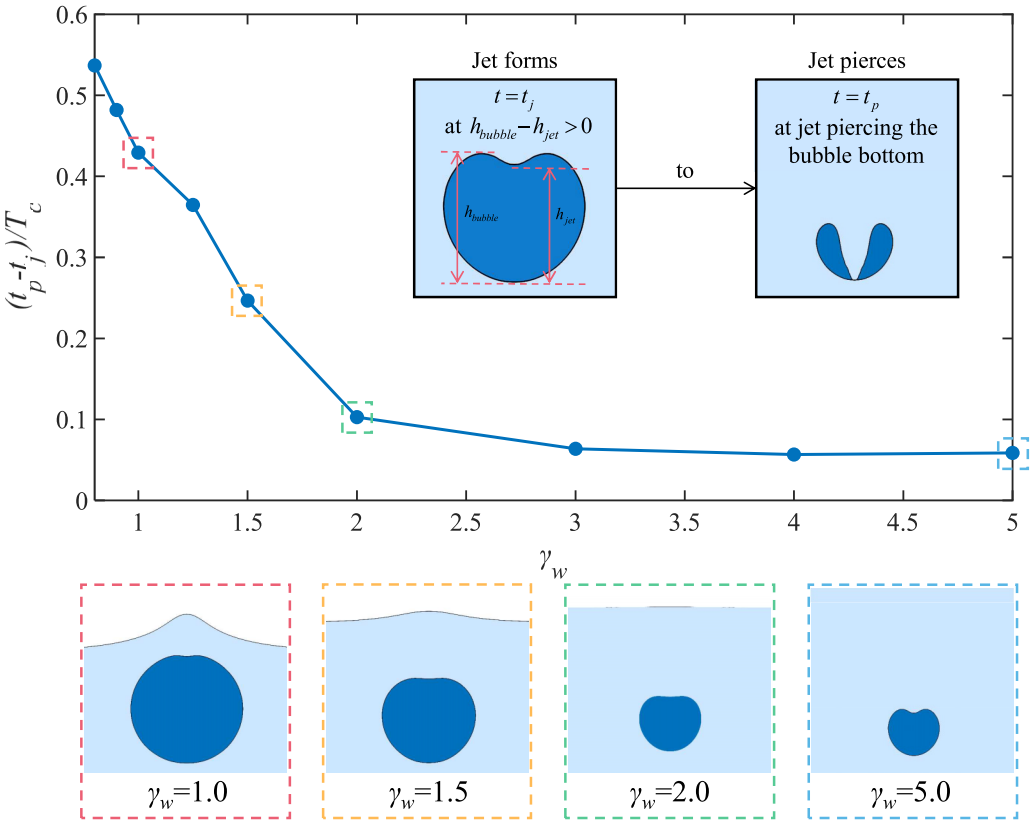

FIG. 9. Variations in the jet duration ($t_p - t_j$) with γ_w at $\gamma_r = 1.5$ obtained from the numerical simulations. The upper right corner shows the definition of the jet duration: from the time of formation (t_j) to the time of piercing the bubble bottom (t_p). The bubble shapes at the jet formation are shown below at four different γ_w. Here the navy and light blue represent the bubble and liquid, respectively.

motion of the jets. The differences appeared in the bubble rebound. The bubbles migrate upward and later downwards during the second cycle in the case of the free vortex [see Fig. 7(a)]. In the case of the wall vortex in the newly expanded regime, the bubble continued migrating downwards [see Fig. 7(b)]. The results revealed that the vortex flow patterns depended principally on the bubble migration during the second cycle. This is determined by the direction of migration $\dot{h}$ at the beginning of the second cycle, that is, at the end of the first cycle. We found that $\dot{h}$ was positive ($\dot{h} > 0$) for the free vortex and negative ($\dot{h} < 0$) for the wall vortex.

B. Mechanism of bubble jetting and vortex flow

Numerical simulations were conducted using OpenFOAM to further analyze the jetting mechanism and subsequent vortex flow induced by the collapse of a cavitation bubble. To verify the accuracy of the simulation, the bubble shape evolutions obtained from the simulations were compared to the experimental observations in the cases of a free vortex and wall vortex. As shown in Fig. 8, the experimental observations in the background and the numerical simulations are represented as blue contours. The contours represent the bubble shape at a volume fraction α of 0.5. Overall, the outer shape of the bubble between the numerical simulations and experimental observations corresponded, including the generation of the free and wall vortex. The numerical simulation method accurately describes the bubble oscillations between the rigid wall and water

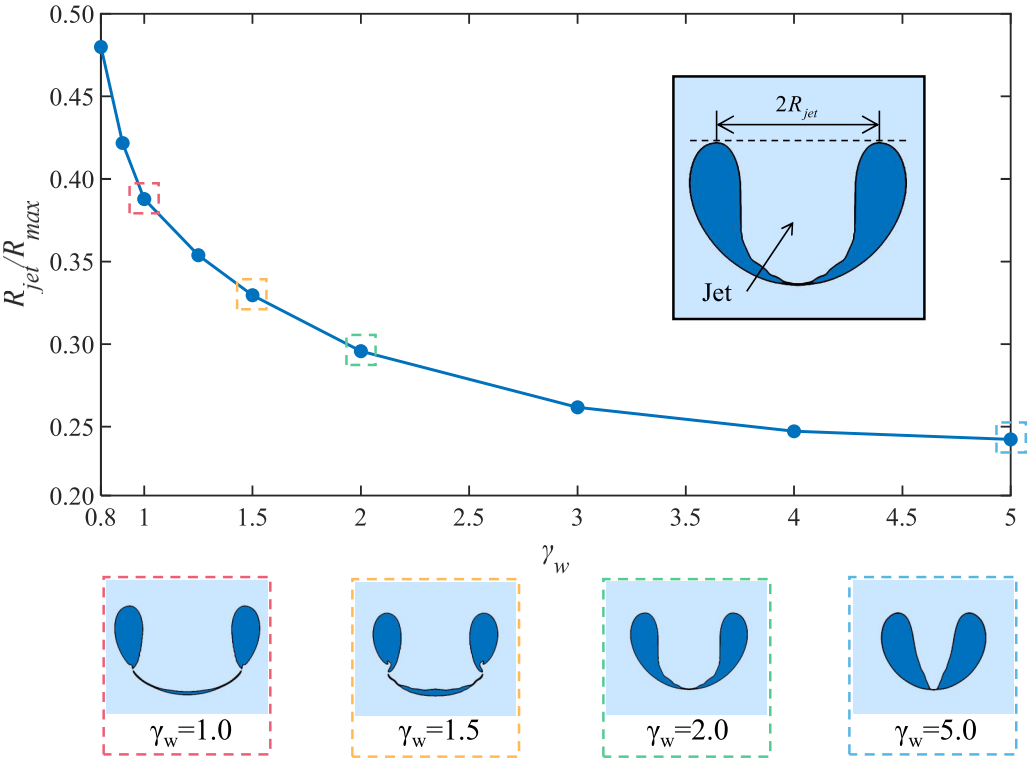

FIG. 10. Variations in the maximum jet radius R_{jet} obtained from the numerical simulations with γ_w at $\gamma_r = 1.5$. The upper right corner shows the definition of the jet radius. The bubble shapes at the jet piercing are shown below at four different γ_w. Here the navy and light blue represent the bubble and liquid, respectively.

surface. The comparisons of the bubble equivalent radius and centroid position between the numerical simulations, theoretical model, and experimental observations are presented in Appendix D.

As aforementioned, the vortex flow patterns were principally determined by the bubble behavior during the oscillations. Bubble shapes and migration are affected by the formation and piercing of the jet. The variations in the jet duration $(t_p - t_j)$ with γ_w at $\gamma_r = 1.5$ obtained from the numerical simulations are shown in Fig. 9. The jet duration is defined as the time interval from the formation t_j to the piercing of the bubble bottom t_p. The jet formation time was determined when the height of the bubble h_{bubble} was greater than that of the jet h_{jet} as shown in the figure. The bubble shapes at the jet formation are shown below for four different γ_w. The jet duration $(t_p - t_j)$ increased as γ_w decreased. This is because the jet was generated earlier during shrinkage owing to the influence of the water surface (see the cases from $\gamma_w = 1.0$ to $\gamma_w = 5.0$). As the influence of the water surface is enhanced, the bubble wall close to it expands easily, and the pressure gradient inducing the jet occurs earlier.

Figure 10 shows the variations in the jet radius R_{jet} obtained from numerical simulations with γ_w at $\gamma_r = 1.5$. R_{jet} is defined as the radius of the cross section of the jet piercing the bubble bottom. The bubble shapes at the jet piercing are shown below for the four different γ_w. As γ_w decreases, R_{jet} increases because a longer jet duration results in a greater radial velocity of the jet. Further, a broader jet is generated during jet piercing. Hence, the constraint of the water surface affects the formation and development of the jet, thereby affecting the subsequent bubble behavior and vortex flow patterns (see Figs. 11 and 12).

Figure 11 shows the flow fields for the formation of a free vortex obtained from the numerical simulations at $\gamma_r = 1$ and $\gamma_w = 2$. In the figure, (1)–(3) represent the first cycle, (4)–(7) the second

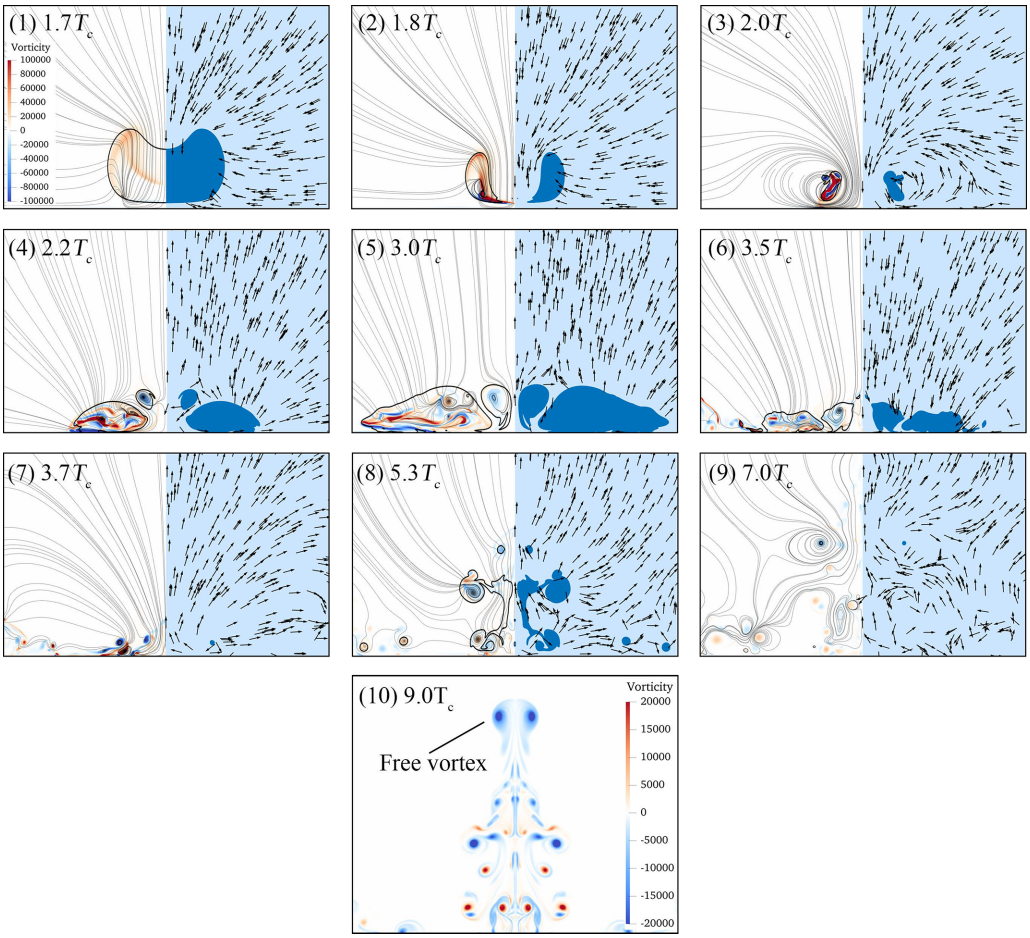

FIG. 11. Flow fields of the formation of a free vortex obtained from the numerical simulations at $\gamma_r = 1$ and $\gamma_w = 2$. In the figure, (1)–(3) represent the first cycle, (4)–(7) the second cycle, (8) and (9) the vortex flow during subsequent oscillations of the bubble, and (10) a global view of the free vortex. In this case, experiment $R_{\max} = 12.21$ mm and $T_c = 1.32$ ms. The vorticity fields and streamlines are shown on the left. The amplitudes of the vorticity are represented by the color bars. The volume fraction fields and velocity vectors are shown on the right. Navy and light blue represent the phases of gas and liquid, respectively.

cycle, (8) and (9) the vortex flow during subsequent oscillations of the bubble, and (10) the global view of the free vortex. Here the jet pierced the bottom of the bubble at $1.8T_c$, and a vortex ring induced by the stagnation flow was observed by the streamlines at $2.0T_c$. The bubble later rebounds with the outwards flow, and the centroid position migrates upward. After $3.0T_c$, the bubble shrank simultaneously in both radial and axial directions during the second cycle, as indicated by the velocity vectors. The inward flows dominated and converged at the origin. Further, an upward flow forms at $3.7T_c$. As the bubbles continued to oscillate, vortex rings migrating upwards were observed in the streamlines at $7.0T_c$. A global view of the free vortex is shown in Fig. 11(10).

Figure 12 shows the flow fields for the formation of a wall vortex in a new expanded regime obtained from the numerical simulations at $\gamma_r = 1$ and $\gamma_w = 1$. Compared to Fig. 11, γ_w decreases, while the influence of the water surface is enhanced in this case. The broader jet pierced at $2.1T_c$. This caused the bubble to expand easily along the wall during the rebound, while the centroid position migrated downwards. Further, the inner toroidal boundary of the bubble begins to contract,

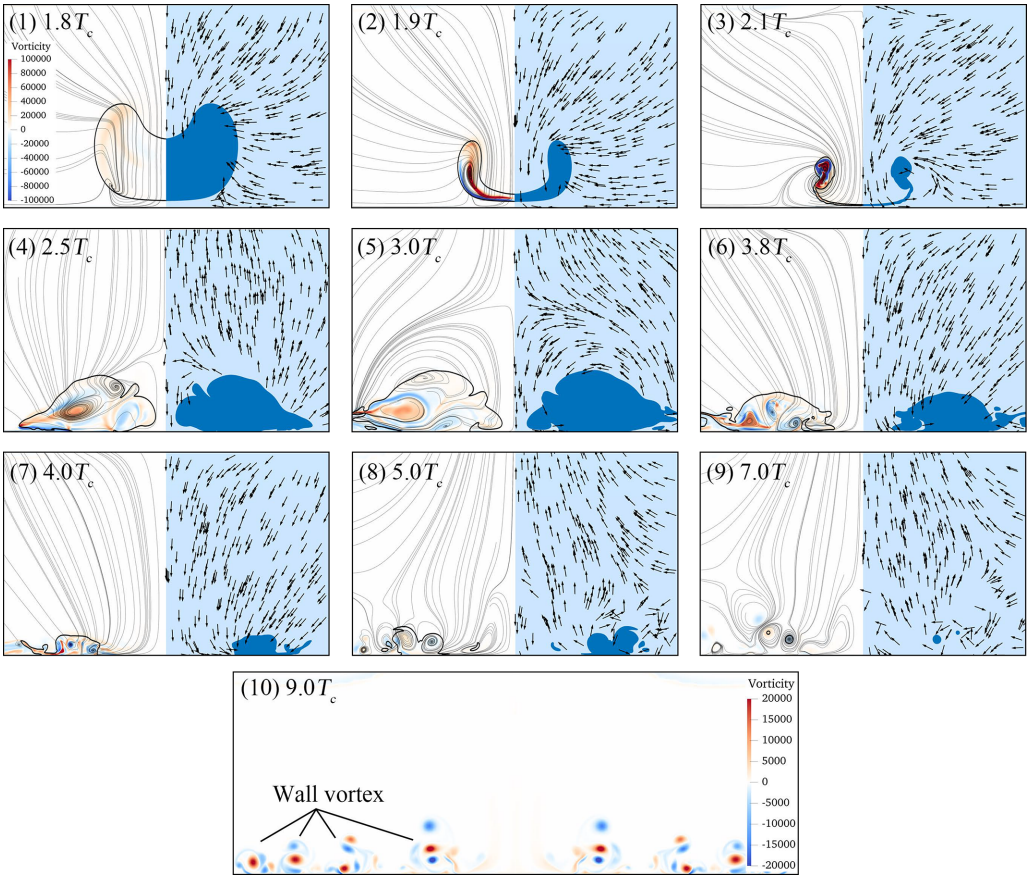

FIG. 12. Flow fields of the formation of a wall vortex in an expanded new regime obtained from the numerical simulations at $\gamma_r = 1$ and $\gamma_w = 1$. In the figure, (1)–(3) represent the first cycle, (4)–(7) the second cycle, (8) and (9) the vortex flow during subsequent oscillations of the bubble, and (10) a global view of the wall vortex. In this case, experiment $R_{\max} = 12.20$ mm and $T_c = 1.12$ ms. The vorticity fields and streamlines are shown on the left. The amplitudes of the vorticity are represented by the color bars. The volume fraction fields and velocity vectors are shown on the right. Navy and light blue represent the phases of gas and liquid, respectively.

whereas the outer boundary expands outwards at $2.5T_c$. The induced downwards flow impacts and moves along the wall during the bubble collapse in the second cycle (see $4.0T_c$). As the bubbles continued to oscillate, outward-migrating vortex rings were observed in the streamlines at $7.0T_c$. A global view of the wall vortex is shown in Fig. 12(10).

C. Criteria and phase diagram for vortex flow patterns

When a bubble is generated between the water surface and rigid wall, the induced broader jet pierces the bottom of the bubble. This causes the bubbles to expand easily along the wall and form a flat shape during the second cycle. The outwards flow dominated during the subsequent oscillations of the bubble. The new regime of the wall vortex was induced by the influence of the water surface. Figure 13 shows a schematic of the vortex flow pattern after the second bubble cycle. As regards a wall vortex near a single rigid wall with a large γ_r, the bubble was relatively far from the wall at the beginning of the second cycle t_c. Here the centroid migrates downwards as the bubble rebounds

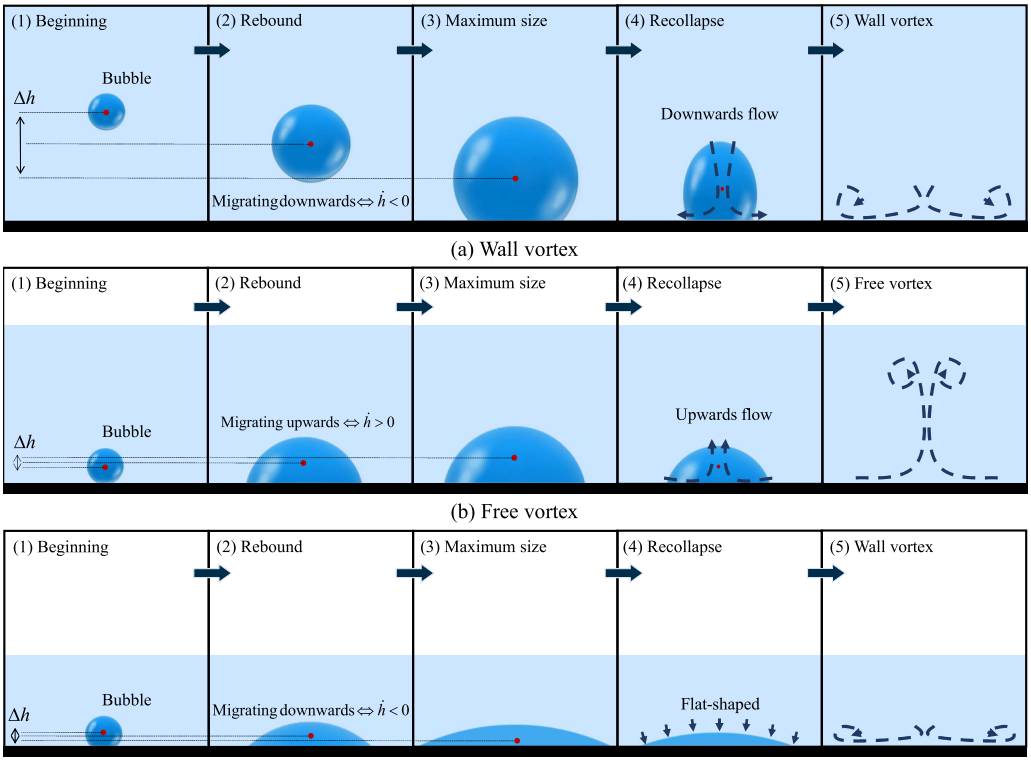

FIG. 13. Schematic of the criteria for the vortex flow patterns after the second bubble cycle: (a) $\dot{h} < 0$ for wall vortex, (b) $\dot{h} > 0$ for the free vortex, and (c) $\dot{h} < 0$ for the wall vortex with the influence of the water surface. Frames (1)–(4) represent the beginning, rebound, maximum size, and collapse of the bubble in the second cycle, while frame (5) represents the vortex flow pattern. The blue arrows represent the directions of the flow. Here R is the bubble radius, h the centroid position, and $\dot{h}$ the direction of centroid migration.

$\dot{h}(t_c) < 0$ and downwards flow dominated in this case. For a free vortex, the bubble centroid migrates upward during the rebound [$\dot{h}(t_c) > 0$], while the upward flow dominates. For a wall vortex in the newly expanded regime, the centroid migrates downwards [$\dot{h}(t_c) < 0$].

Consequently, the vortex flow patterns can be determined by the migration of the bubble at the beginning of the second cycle, that is, at the end of the first cycle (t_c). The direction of the centroid migration $\dot{h}(t_c)$ represents the direction of the system momentum at t_c because the radial motion can be ignored. Consequently, the criteria for vortex flow patterns are proposed based on $\dot{h}(t_c)$ at t_c. A free vortex is formed at $\dot{h}(t_c) < 0$, while $\dot{h}(t_c) > 0$ is formed for a wall vortex. The criteria expressions are summarized as follows:

$$\begin{aligned} &\text{Free vortex:} \quad \dot{h}(t) > 0, \quad \text{at} \quad t = t_c \\ &\text{Wall vortex:} \quad \dot{h}(t) < 0, \quad \text{at} \quad t = t_c \end{aligned} \tag{21}$$

A theoretical model was solved to obtain the bubble radius and centroid position at different standoff distances. By combining these criteria, a phase diagram of the vortex flow patterns was obtained, as shown in Fig. 14. In the figure, the orange area represents the free vortex regime, the blue the wall vortex, and the navy blue the new regime expanded by the water surface. At $\gamma_w > 4$, the constraint on the water surface barely affected the bubble dynamics and vortex flow. A free vortex transition into a wall vortex as γ_r increases, as in the case of a single rigid wall. At $0.85 < \gamma_w < 4$,

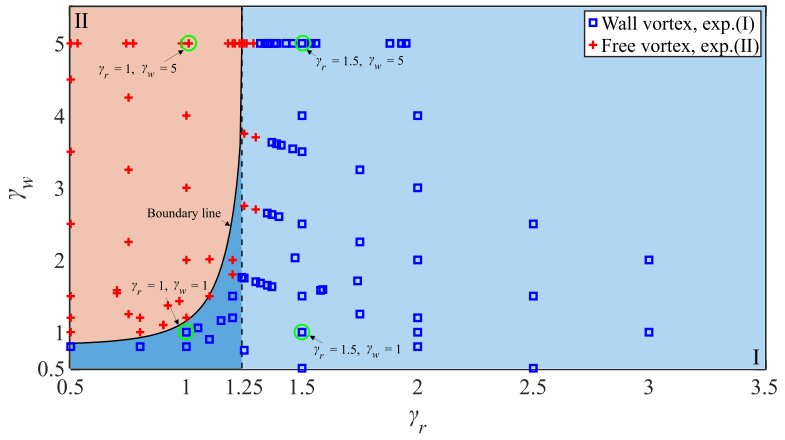

FIG. 14. Phase diagram of the vortex flow induced by the oscillations of a cavitation bubble between a water surface and rigid wall. The plus and square represent the experimental observations of the free vortex and wall vortex, respectively. The orange and blue areas are obtained by solving the theoretical model. The orange area indicates the free vortex regime. The blue area represents the wall vortex, wherein the navy blue area represents the expanded new regime by the water surface. At $\gamma_w < 4$, the formation and development of the vortex flow are affected by the constraint of the water surface.

the wall vortex in the new expanded regime arises owing to the influence of the water surface. When $0.5 < \gamma_w < 0.85$, no free vortex occurred as γ_r decreased and was completely replaced by the wall vortex. Consequently, the boundary line between the free and wall vortex regime becomes an exponential function instead of a straight line in the case of a single rigid wall. The introduction of the water surface enlarged the wall vortex regime. The wall vortex was generated at a smaller γ_r value.

The experimentally obtained results are plotted in a phase diagram for comparison. The plus and square symbols represent the experimental observations of the free and wall vortices, respectively. The free vortex regime determined through experimental observations was slightly larger than that obtained using the theoretical model. This is because higher-order quantities were neglected in the theoretical model to simplify the deduction of the velocity potential. Overall, the theoretical estimates correspond with the experimental observations.

According to Reuter *et al.* [3] and Zeng *et al.* [5], the shear stress induced by the vortex flows is important in engineering applications. Reuter *et al.* [3] observed that a wall vortex was generated at $\gamma_r > 1.3$. Our study revealed that the introduction of a water surface expanded the wall-vortex formation regime. To further evaluate its potential for different applications, we numerically investigated the spatiotemporal distribution of the wall shear stress induced by different vortex flows, as shown in Fig. 15. Figure 15(a) shows the free vortex, Fig. 15(b) the wall vortex, and Figs. 15(c) and 15(d) the wall vortex under the influence of a water surface. In the spatiotemporal distributions, the first colored bar represents the inward shear stress (towards the axis of symmetry), whereas the second represents the outwards shear stress (away from the axis of symmetry). The wall shear stress was obtained as $\tau = \mu d\boldsymbol{U}/dy$ at $y < \epsilon$, wherein ϵ is the thickness of the region with a constant shear rate located within the boundary layer. As shown in Figs. 15(a)–15(d), the jet impacted the rigid wall, thereby producing a high outwards shear stress after the first collapse of the cavitation bubble. After the second bubble cycle, the wall shear stress was principally induced by the vortex flow. Comparing Figs. 15(a) to 15(b), the wall vortex has a higher wall shear stress (125.89 kPa) after $t = 4T_c$ and the area is extended to $1.21R_{\max}$, while a maximum of 25.12 kPa for free vortex. This suggests that the wall vortex has a greater potential for applications such as ultrasonic cleaning. As regards the wall vortex with the influence of the water surface, the maximum wall shear stress

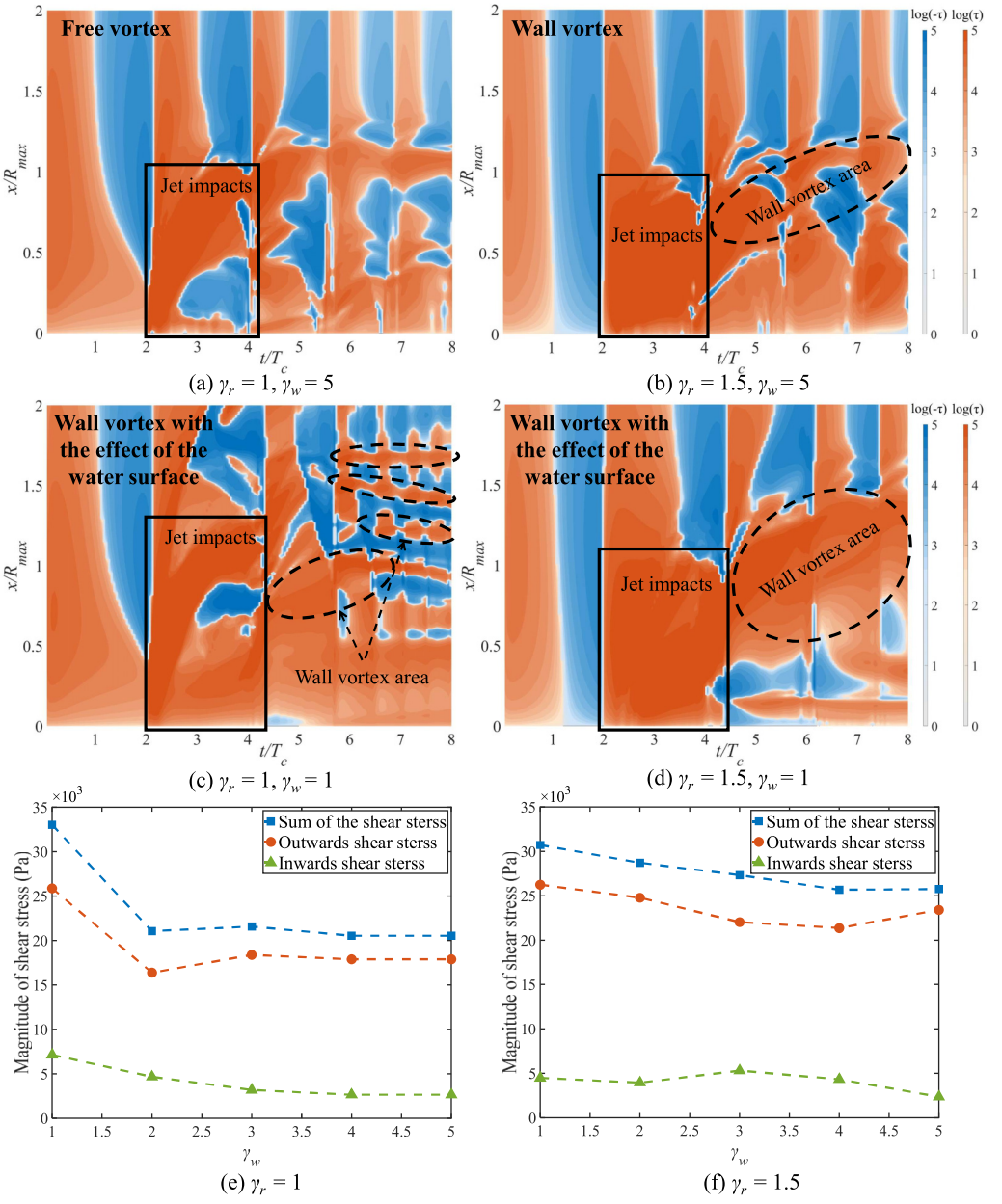

FIG. 15. Comparisons of the spatiotemporal distributions of the wall shear stress: (a) free vortex, (b) wall vortex, and [(c) and (d)] wall vortex with the influence of the water surface. The influence of the water surface on the sum of the shear stress is shown in (e) and (f). In the spatiotemporal distributions [(a)–(d)], the first color bar represents the inwards shear stress (towards the axis of symmetry), while the second represents the outwards shear stress (away from the axis of symmetry).

is 120.23 kPa and the area increases up to $1.74R_{\max}$ in Fig. 15(c), while in Fig. 15(d) it reaches a maximum of 143.88 kPa and an area of $1.48R_{\max}$. The comparisons between Figs. 15(a) and 15(c) and Figs. 15(b) and 15(d) suggest that the wall vortex with the influence of the water surface produces a larger shear stress area and higher wall shear stress.

We investigated the sum of the shear stresses induced by the vortex flow, as shown in Figs. 15(e) and 15(f). The sum of the shear stresses was calculated by integrating the shear stress in the vortex area as $1/(x_{\max}t_{\max})\int_t\int_x(\mu d\boldsymbol{U}/dy)dxdt$ at $y < \epsilon$. The blue squares indicate the sum of the outwards and inward shear stresses. The orange circles and green triangles indicate the sum of the outwards and inward shear stresses, respectively. As γ_w decreases, the sum of the shear stresses increases from 20.52 to 33.00 kPa at $\gamma_r = 1$, and increases from 25.76 to 30.73 kPa at $\gamma_r = 1.5$. As the influence of the water surface was enhanced, the outwards and inward shear stresses increased.

IV. CONCLUSIONS

In this study, we found that the introduction of a water surface expands the wall vortex regime; that is, a wall vortex forms instead of a free vortex at a smaller γ_r value. The wall vortex in the newly expanded regime was investigated using a combination of laboratory experiments, numerical simulations, and theoretical modeling. Owing to the influence of the water surface, a broader jet pierced the bottom of the bubble. This caused the bubbles to expand easily along the wall and form a flat shape during the second cycle. Hence, an outwards flow formed instead of an upward flow after the bubble recollapsed.

Experimental observations revealed that the vortex flow patterns depend principally on bubble migration during the second cycle. The criteria for the vortex flow patterns were proposed based on the direction of the centroid migration $\dot{h}(t_c)$ of the bubble at the beginning of the second cycle t_c. The direction of the centroid migration $\dot{h}(t_c)$ represents the direction of the system momentum at t_c because the radial motion can be ignored. Hence, a free vortex occurs when the upward flow dominates [$\dot{h}(t_c) > 0$], while the downwards flow dominates the wall vortex [$\dot{h}(t_c) < 0$].

A theoretical model was developed using a Lagrangian formulation to describe the bubble radius and centroid position between the boundaries. In the model, image theory was used to obtain expressions for the velocity potential, and two infinite sets were obtained to satisfy the boundary conditions of the water surface and rigid wall. Based on these criteria, a phase diagram of the vortex flows was obtained by solving a theoretical model. The boundary line between the free and wall vortex regime becomes an exponential function instead of a straight line in the case of a single rigid wall. The theoretical estimates correspond with the experimental observations.

We numerically investigated the spatiotemporal distributions of the wall shear stress induced by different vortex flows. The analysis suggests that the wall vortex has a greater potential for applications such as ultrasonic cleaning. When introducing a water surface, no free vortex occurs as γ_r decreases and is completely replaced by the wall vortex at $0.5 < \gamma_w < 0.85$. Furthermore, the wall vortex under the influence of the water surface produces a larger shear stress area and higher wall shear stress. The findings of this study provide new insights for engineering applications such as ultrasonic cleaning, sonoporation, drug delivery, and laser surgery.

ACKNOWLEDGMENTS

The authors gratefully acknowledge the group of Professor Zhang (Harbin Engineering University) for supplying the electric discharge machines. This work was supported by the National Natural Science Foundation of China (12122214, 12272382, 12293000, 12293003, and 12293004), the Youth Innovation Promotion Association CAS (2022019), and the High-level Innovation Research Institute Program of Guangdong Province (No. 2020B0909010003 and GARA2022002000).

APPENDIX A: DETAILS OF IMAGE PROCESSING

The bubble equivalent radius was calculated from the equivalent area using the gray values in the image based on OpenCV [39]. As shown in Fig. 16, the original image is first extracted in grayscale. Further, a region-filling process is used to obtain the equivalent area of the bubble. The equivalent volume (V) is calculated by integrating the equivalent area around the symmetric axis. The bubble

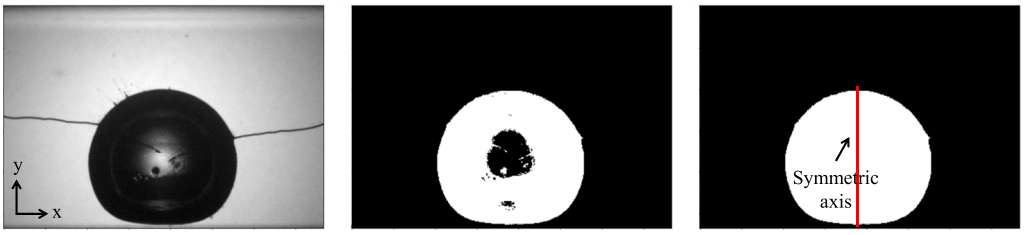

FIG. 16. Details of the gray value processes by OpenCV: From the original image to the region filling. The original image is from experiment observations. The red lines represent the symmetric axis of the bubble.

equivalent radius (R) was obtained from $V = 4/3\pi R^3$ assuming that the bubble remained spherical during the oscillations. The bubble centroid (h) is determined using $h = \int ydxdy / \int dxdy$.

APPENDIX B: DETAILED DERIVATION PROCESS OF THEORETICAL MODEL

The velocity potential function of an inviscid, irrotational, and incompressible liquid flow field satisfies Laplace's equation

$$\nabla^2\phi = 0. \tag{B1}$$

The velocity potential of the ith isolated bubble with the boundary conditions corresponding to an infinite liquid is expressed as follows:

$$\phi_i = -\frac{R_i^2}{r_i}\dot{R}_i - \frac{R_i^3}{2r_i^2}\boldsymbol{U}_i \cdot \boldsymbol{n}_i. \tag{B2}$$

In a system with m multiple interacting bubbles, the velocity potential is expressed as follows:

$$\phi^0 = \sum_m \phi_m^0. \tag{B3}$$

This equation did not satisfy the boundary conditions for multiple bubbles; hence, the equation was corrected. The Taylor expansion for the velocity potential near the ith bubble is expressed as follows:

$$\phi^0(\boldsymbol{r}_i) = \phi_i^0(\boldsymbol{r}_i) + \sum_{m\neq i}\phi_m^0(\boldsymbol{r}_{mi} + \boldsymbol{r}_m) = \phi_i^0(\boldsymbol{r}_i) + \sum_{m\neq i}\left[\phi_m^0(\boldsymbol{r}_{mi}) + \boldsymbol{c}_{mi}\cdot\boldsymbol{r}_m + \cdots\right], \tag{B4}$$

where $\boldsymbol{r}_{mi} = \boldsymbol{r}_i - \boldsymbol{r}_m$ and $\boldsymbol{c}_{mi}$ are calculated by differentiating the velocity potential,

$$\boldsymbol{c}_{mi} = \left[\frac{\partial\phi_m(\boldsymbol{r}_m)}{\partial r_m}\right] = \frac{R_m^2}{r_{mi}^2}\dot{R}_m\boldsymbol{n}_{mi} - \frac{R_m^3}{2r_{mi}^3}[\boldsymbol{U}_m - 3(\boldsymbol{U}_m\cdot\boldsymbol{n}_{mi})\boldsymbol{n}_{mi}]. \tag{B5}$$

A comparison reveals that the term $\boldsymbol{c}_{mi}\cdot\boldsymbol{r}_m$ is a problem wherein the boundary conditions are not satisfied for the ith bubble. Further corrections were made to the velocity potential. It is assumed that the modified velocity potential ϕ' satisfies the Laplace equation. Hence,

$$\phi(\boldsymbol{r}_i) = \phi^0(\boldsymbol{r}_i) + \phi'(\boldsymbol{r}_i). \tag{B6}$$

The corresponding expansion for the corrected velocity potential is expressed as follows:

$$\phi'(\boldsymbol{r}_i) = \phi_i'(\boldsymbol{r}_i) + \sum_{m\neq i}\phi_m'(\boldsymbol{r}_{mi} + \boldsymbol{r}_m) = \phi_i'(\boldsymbol{r}_i) + \sum_{m\neq i}[\phi_m'(\boldsymbol{r}_{mi}) + \boldsymbol{d}_{mi}\cdot\boldsymbol{r}_m + \cdots], \tag{B7}$$

where

$$\phi_i'(\boldsymbol{r}_i) = \sum_{m\neq i} \frac{R_i^3}{2r_i^2}\boldsymbol{c}_{mi}\cdot\boldsymbol{n}_i, \tag{B8}$$

$$\phi_m'(\boldsymbol{r}_{mi}) = \sum_{m\neq i} \frac{R_m^3}{2r_{mi}^2}\boldsymbol{c}_{im}\cdot\boldsymbol{n}_{mi}. \tag{B9}$$

The correction is truncated by neglecting the small quantities above the fourth order to obtain the velocity potential function as expressed as follows:

$$\phi(\boldsymbol{r}_i) = \phi_i^0(\boldsymbol{r}_i) + \phi_i'(\boldsymbol{r}_i) + \sum_{m\neq i}\left[\phi_m^0(\boldsymbol{r}_{mi}) + \phi_m'(\boldsymbol{r}_{mi}) + \boldsymbol{c}_{mi}\cdot\boldsymbol{r}_m\right]. \tag{B10}$$

The velocity potential of the ith bubble surface is obtained by solving the following velocity potential function:

$$\begin{aligned}\phi\mid_{S_i} = &-\left(R_i\dot{R}_i + \frac{R_i}{2}\boldsymbol{U}_i\cdot\boldsymbol{n}_i\right) + \sum_{m,m\neq i}\left\{-\left(\frac{R_m^2}{r_{im}}\dot{R}_m + \frac{R_m^3}{2r_{im}^2}\boldsymbol{U}_m\cdot\boldsymbol{n}_{mi}\right) + \frac{3R_iR_m^2}{2r_{im}^2}\dot{R}_m(\boldsymbol{n}_{mi}\cdot\boldsymbol{n}_i)\right.\\ &\left. - \frac{3R_iR_m^3}{4r_{im}^3}[\boldsymbol{U}_m\cdot\boldsymbol{n}_i - 3(\boldsymbol{U}_m\cdot\boldsymbol{n}_{mi})(\boldsymbol{n}_{mi}\cdot\boldsymbol{n}_i)]\right\} + \sum_{j,m,m\neq i,j}\frac{R_j^2R_m^2}{2r_{im}^2r_{jm}^2}\cdot R_j(\boldsymbol{n}_{jm}\cdot\boldsymbol{n}_{mi}),\end{aligned} \tag{B11}$$

according to the following equation:

$$\int_{S_i}(\boldsymbol{a}\cdot\boldsymbol{n}_i)(\boldsymbol{b}\cdot\boldsymbol{n}_i)dS_i = \frac{4\pi}{3}R_i^2(\boldsymbol{a}\cdot\boldsymbol{b}), \tag{B12}$$

$$\int_{S_i}(\boldsymbol{n}_i)dS_i = 0. \tag{B13}$$

The kinetic energy of the flow field for the interaction of multiple bubbles is obtained by substituting the velocity potential into the kinetic energy expression in Eq. (2) as expressed as follows:

$$\begin{aligned}K = 2\pi\rho\Bigg\{&\sum_i R_i^3\dot{R}_i^2 + \frac{1}{6}\sum_i R_i^3U_i^2 + \sum_{i,m,i\neq m}\frac{2R_i^2R_m^2}{r_{im}}\dot{R}_i\dot{R}_m\\ &+ \sum_{i,m,i\neq m}\frac{R_i^2R_m^2}{r_{im}^2}[R_i\dot{R}_m(\boldsymbol{U}_i\cdot\boldsymbol{n}_{im}) + R_m\cdot R_i(\boldsymbol{U}_m\cdot\boldsymbol{n}_{mi})]\\ &+ \frac{1}{2}\sum_{i,m,i\neq m}\frac{R_i^3R_m^3}{r_{im}^3}[(\boldsymbol{U}_i\cdot\boldsymbol{U}_m) - 3(\boldsymbol{U}_i\cdot\boldsymbol{n}_{im})(\boldsymbol{U}_m\cdot\boldsymbol{n}_{mi})]\\ &+ \sum_{i,j,m,m\neq i,j}\frac{R_i^2R_j^2R_m^3}{r_{im}^2r_{jm}^2}\dot{R}_i\dot{R}_j(\boldsymbol{n}_{jm}\cdot\boldsymbol{n}_{im})\Bigg\}.\end{aligned} \tag{B14}$$

As regards the image system, the boundary conditions for the positive image bubble R_p and negative image bubble R_n are expressed as follows:

$$\frac{\partial\phi}{\partial r_p} = \dot{R}_p + \boldsymbol{U}_p\cdot\boldsymbol{n}_p, \quad \text{at } r_p = R_p. \tag{B15}$$

$$\frac{\partial\phi}{\partial r_n} = -\dot{R}_n + \boldsymbol{U}_n\cdot\boldsymbol{n}_n, \quad \text{at } r_n = R_n. \tag{B16}$$

Considering the influence of the image bubbles on the initial bubble R_0, we substitute the velocity potentials of the image bubbles and boundary conditions into the equation for the kinetic energy of

the flow field (preserved to second order) as expressed as follows:

$$K = 2\pi\rho\left\{R_0^3\dot{R}_0^2 + \frac{1}{6}R_0^3U_0^2 + 2R_0^4\dot{R}^2\sum_{k=0}(-1)^k(\mathcal{A}_k - \mathcal{B}_k)\right.$$
$$\left. + R_0^5\dot{R}(\boldsymbol{U}_0\cdot\boldsymbol{n}_{0k})\sum_{k=0}(-1)^k\left(\mathcal{A}_k^2 + \mathcal{B}_k^2\right)\right\}, \tag{B17}$$

where

$$\mathcal{A}_k = \frac{1}{2}\frac{1}{(k+1)(h_r+h_w) - h_w}, \tag{B18}$$

$$\mathcal{B}_k = \frac{1}{2}\frac{1}{k(h_r+h_w) + h_w}, \tag{B19}$$

according to the Lagrangian formulation,

$$L(\boldsymbol{x}, \dot{\boldsymbol{x}}, t) = K(\boldsymbol{x}, \dot{\boldsymbol{x}}, t) - V(\boldsymbol{r}). \tag{B20}$$

The terms in the Lagrange equations are as follows:

$$\frac{d}{dt}\left(\frac{\partial L}{\partial \dot{R}}\right) = 2\pi\rho\left[6R_0^2\dot{R}_0^2 + 2R_0^3\ddot{R}_0 + \left(8R_0^3\dot{R}_0^2 + 2R_0^4\ddot{R}_0\right)\sum_{k=0}(-1)^k(\mathcal{A}_k - \mathcal{B}_k)\right] - \frac{P - P_\infty}{\rho}, \tag{B21}$$

$$\frac{\partial L}{\partial R} = 2\pi\rho\left[3R_0^2\dot{R}_0^2 + \frac{1}{2}R_0^2U_0^2 + 4R_0^3\dot{R}_0^2\sum_{k=0}(-1)^k(\mathcal{A}_k - \mathcal{B}_k)\right], \tag{B22}$$

$$\frac{d}{dt}\left(\frac{\partial L}{\partial \dot{\boldsymbol{r}}}\right) = 2\pi\rho\left[R_0^2\dot{R}_0U_0 + \frac{1}{3}R_0^3\dot{U}_0 - \left(5R_0^4\dot{R}_0^2 + R_0^5\ddot{R}_0\right)\sum_{k=0}(-1)^k\left(\mathcal{A}_k^2 + \mathcal{B}_k^2\right)\right], \tag{B23}$$

$$\frac{\partial L}{\partial \boldsymbol{r}} = 2\pi\rho\left[-2R_0^4\dot{R}_0^2\sum_{k=0}(-1)^k\left(\mathcal{A}_k^2 + \mathcal{B}_k^2\right)\right]. \tag{B24}$$

The equations of motion for a bubble between a rigid wall and water surface are expressed as follows:

$$\ddot{R} = \frac{\frac{P-P_\infty}{\rho} + \frac{1}{4}U^2 - \frac{3}{2}\dot{R}^2\left[1 + \frac{4R}{3}\sum_{k=0}(-1)^k(\mathcal{A}_k - \mathcal{B}_k)\right]}{\left[R + R^2\sum_{k=0}(-1)^k(\mathcal{A}_k - \mathcal{B}_k)\right]}, \tag{B25}$$

$$\ddot{h} = \dot{U} = -\frac{3\dot{R}U}{R} + \frac{9R\dot{R}^2 + 3R^2\ddot{R}}{4}\sum_{k=0}(-1)^k\left(\mathcal{A}_k^2 + \mathcal{B}_k^2\right). \tag{B26}$$

When the bubble is in an unbounded liquid (without migration), the radial motion equation is transformed into the Rayleigh-Plesset equation as expressed as follows:

$$R\ddot{R} + \frac{3}{2}\dot{R}^2 = \frac{P - P_0}{\rho}. \tag{B27}$$

APPENDIX C: VERIFICATION OF NUMERICAL SIMULATIONS

Three grids with different numbers of nodes are used to verify the grid independence of the simulations. Grids with 420 000, 580 000, and 810 000 nodes were considered and referred to as coarse, medium, and fine grids, respectively. The initial conditions of the bubble for numerical simulations (R_0 and p_{in0}) are uniquely determinable based on the experimental observations. Here the initial radius of the bubble R_0 is determined based on the size of the copper wires. It is set as $R_0 = 1$ mm, which is slightly larger than the crossing point of two 0.3-mm diameter electrodes. The

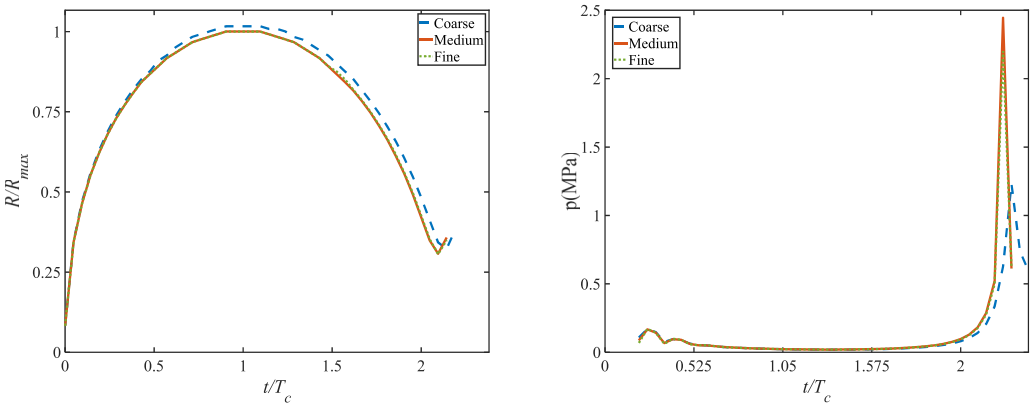

FIG. 17. Variations in the bubble radius (a) and wall pressure below the bubble centroid (b) for three different grids at $\gamma_r = 1.5$ and $\gamma_w = 1.5$. The three grids are a coarse grid, medium grid, and fine grid with 420 000, 580 000, and 810 000 nodes, respectively.

initial internal pressure $p_{\text{in0}} = 84$ MPa is then determined from the maximum bubble radius $R_{\max}$ and time when the bubble reaches the maximum size T_c, which are obtained from experimental observations. The other settings in the simulations are as follows: dynamic viscosity of the liquid $\mu_l = 8.545\times10^{-4}$ Pa s, dynamic viscosity of the gas $\mu_g = 1.840\times10^{-5}$ Pa s, specific heat capacity of the liquid $C_{pl} = 4195\,\text{J}\,\text{kg}^{-1}\,\text{K}^{-1}$, specific heat capacity of the gas $C_{pg} = 1007\,\text{J}\,\text{kg}^{-1}\,\text{K}^{-1}$, and surface tension $\sigma = 0.07\,\text{N}\,\text{m}^{-1}$. As compared to the nonspherical collapse near boundaries, the thermal and mass transfer effects are more pronounced in the case of spherical bubble collapses. Meanwhile, the formation of the vortex flow is mainly due to the movement of the jet, indicating that the thermal and mass transfer effects are not significant in these processes. Thus, the thermal effects and mass transfer are neglecting.

Figure 17 shows the variations in the bubble radius and wall pressure below the bubble centroid over time for the three grids at $\gamma_r = 1.5$ and $\gamma_w = 1.5$. The results obtained with the coarse grid exhibited some differences from the others in the later stages of the first cycle, whereas the results of the medium and fine grids were consistent in terms of the evolution of the bubble radius and wall pressure. As regards the coarse grid, the maximum errors in the radius, pressure, and collapse time were 1.15%, 11.1%, and 2.08%, respectively. Hence, we used a medium grid of 580 000 nodes in all the simulations to balance the simulation accuracy and computational efficiency.

APPENDIX D: VERIFICATION OF THEORETICAL MODEL

The influence of the image bubbles on the original bubble decreased with the distance. Hence, finite sets of image bubbles are used to approximate infinite sets to obtain solutions for the theoretical model. We compared the radial and centroid migrations for the different numbers of image bubbles. The fourth-order Runge-Kutta algorithm is used to solve the theoretical model. The atmospheric pressure was $P_\infty = 10^5$ Pa. The specific heat ratio of the gas was $\kappa = 1.4$ and the vapor pressure was $P_v = 2300$ Pa. Figure 18 compares the theoretical results for the $\gamma_r = 1.5$ and $\gamma_w = 2.5$ for different numbers of image bubbles. Here $k = 1$, 2, 3, and 4 represent 5, 9, 13, and 17 image bubbles, respectively. The enlarged areas are represented by the green boxes. As k increases, the results approach those of the infinite sets, while the maximum relative deviations of the results decrease. These are 10.92%, 5.87%, and 1.99% for the bubble radius and 3.95%, 2.46%, and 0.73% for the centroid position. Hence, it is reasonable to use the 13 image bubbles ($k = 3$) from the finite sets to approximate the infinite sets.

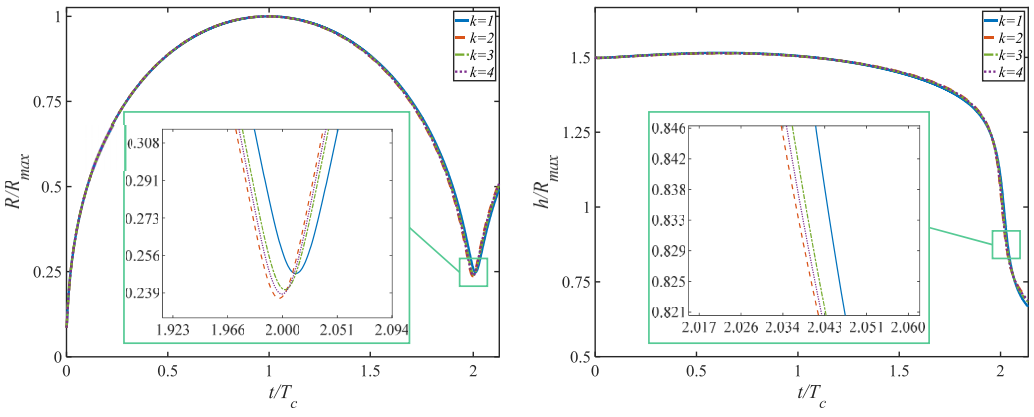

FIG. 18. Comparisons of the theoretical results at $\gamma_r = 1.5$ and $\gamma_w = 2.5$ for different numbers of image bubbles: The (a) bubble radius R and (b) centroid position h. $k = 1$, 2, 3, and 4 represent 5, 9, 13, and 17 image bubbles, respectively. The enlarged areas are shown in green boxes.

Figure 19 shows a comparison of the bubble radius and centroid position between the numerical simulations, theoretical model, and experimental observations during the first oscillation. The open symbols, solid lines, and dotted lines represent the experimental observations, theoretical solutions, and simulation results, respectively. As shown in Fig. 19, the errors in the maximum radius are 0.10% for $\gamma_r = 1.5$ and $\gamma_w = 2.5$, 0.06% for $\gamma_r = 1$ and $\gamma_w = 2$ between the experimental observations and numerical results, and 0.54% and 0.93% between the experimental observations and theoretical solutions. Some differences in the centroid positions appeared at a later stage of collapse. One reason for this deviation is that higher-order quantities were neglected to simplify the derivation of the theoretical model. Overall, the numerical simulation method and theoretical model accurately described the dynamics of the bubble between a rigid wall and the water surface.

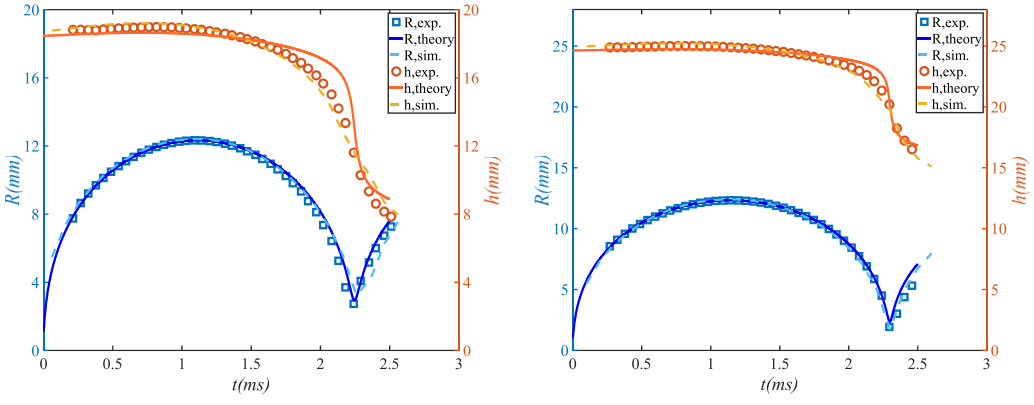

FIG. 19. Comparison of the bubble radius and centroid position between the numerical simulations, theoretical model, and experimental observations during the first oscillation: (a) $\gamma_r = 1.5$ and $\gamma_w = 2.5$ and (b) $\gamma_r = 2$ and $\gamma_w = 3$. The open symbols represent the experimental observations, solid lines the theoretical solutions, and dotted lines the simulation results.

[1] N. K. Bourne and J. E. Field, Shock-induced collapse of single cavities in liquids, J. Fluid Mech. **244**, 225 (1992).
[2] G. Bark and R. E. Bensow, Hydrodynamic mechanisms controlling cavitation erosion, Int. Shipbuild. Progr. **60**, 345 (2013).
[3] F. Reuter, S. R. Gonzalez-Avila, R. Mettin, and C. D. Ohl, Flow fields and vortex dynamics of bubbles collapsing near a solid boundary, Phys. Rev. Fluids **2**, 064202 (2017).
[4] R. Dijkink, S. Le Gac, E. Nijhuis, A. van den Berg, I. Vermes, A. Poot, and C. D. Ohl, Controlled cavitation-cell interaction: Trans-membrane transport and viability studies, Phys. Med. Biol. **53**, 375 (2008).
[5] Q. Y. Zeng, S. R. Gonzalez-Avila, R. Dijkink, P. Koukouvinis, M. Gavaises, and C. D. Ohl, Wall shear stress from jetting cavitation bubbles, J. Fluid Mech. **846**, 341 (2018).
[6] Q. Y. Zeng, H. J. An, and C. D. Ohl, Wall shear stress from jetting cavitation bubbles: Influence of the stand-off distance and liquid viscosity, J. Fluid Mech. **932**, A14 (2021).
[7] W. Eisenmenger, The mechanisms of stone fragmentation in eswl, Ultrasound Med. Biol. **27**, 683 (2001).
[8] C. D. Ohl, M. Arora, R. Dijkink, V. Janve, and D. Lohse, Surface cleaning from laser-induced cavitation bubbles, Appl. Phys. Lett. **89**, 074102 (2006).
[9] F. Reuter, S. Lauterborn, R. Mettin, and W. Lauterborn, Membrane cleaning with ultrasonically driven bubbles, Ultrason. Sonochem. **37**, 542 (2017).
[10] N. U. Jin, F. H. Zhang, Y. Cui, L. Sun, H. X. Gao, Z. Pu, and W. M. Yang, Environment-friendly surface cleaning using micro-nano bubbles, Particuology **66**, 1 (2022).
[11] M. Kornfeld and L. Suvorov, On the destructive action of cavitation, J. Appl. Phys. **15**, 495 (1944).
[12] M. S. Plesset and R. B. Chapman, Collapse of an initially spherical vapour cavity in neighbourhood of a solid boundary, J. Fluid Mech. **47**, 283 (1971).
[13] Z. Wang, P. Xu, Z. Ren, L. Yu, Z. Zuo, and S. Liu, Dynamics of cavitation bubbles in viscous liquids in a tube during a transient process, Ultrason. Sonochem. **104**, 106840 (2024).
[14] A. M. Zhang, X. L. Yao, and L. H. Feng, The dynamic behavior of a gas bubble near a wall, Ocean Eng. **36**, 295 (2009).
[15] S. Li, S. P. Wang, A. M. Zhang, and Iop, Bubble jet impact on a rigid wall of different stand-off parameters, in *International Symposium on Cavitation and Multiphase Flow (ISCM)*, IOP Conference Series—Materials Science and Engineering Vol. 72 (IOP, Bristol, UK, 2015), p. 022010.
[16] O. Supponen, D. Obreschkow, M. Tinguely, P. Kobel, N. Dorsaz, and M. Farhat, Scaling laws for jets of single cavitation bubbles, J. Fluid Mech. **802**, 263 (2016).
[17] C. Lechner, W. Lauterborn, M. Koch, and R. Mettin, Fast, thin jets from bubbles expanding and collapsing in extreme vicinity to a solid boundary: A numerical study, Phys. Rev. Fluids **4**, 021601(R) (2019).
[18] C. Lechner, W. Lauterborn, M. Koch, and R. Mettin, Jet formation from bubbles near a solid boundary in a compressible liquid: Numerical study of distance dependence, Phys. Rev. Fluids **5**, 093604 (2020).
[19] F. Reuter and C. D. Ohl, Supersonic needle-jet generation with single cavitation bubbles, Appl. Phys. Lett. **118**, 134103 (2021).
[20] F. Reuter, Q. Y. Zeng, and C. D. Ohl, The rayleigh prolongation factor at small bubble to wall stand-off distances, J. Fluid Mech. **944**, A11 (2022).
[21] Z. Ren, H. Han, H. Zeng, C. Sun, Y. Tagawa, Z. Zuo, and S. Liu, Interactions of a collapsing laser-induced cavitation bubble with a hemispherical droplet attached to a rigid boundary, J. Fluid Mech. **976**, A11 (2023).
[22] A. M. Zhang, S. M. Li, P. Cui, S. Li, and Y. L. Liu, A unified theory for bubble dynamics, Phys. Fluids **35**, 033323 (2023).
[23] Q. Yi, P. Guo, Z. Zuo, and S. Liu, Modeling ofvapor bubble dynamics considering the metastable fluid state, Phys. Fluids **36**, 023326 (2024).
[24] J.-Z. Wang, G.-H. Wang, Q.-Y. Zeng, and Y.-W. Wang, Recent progress on the jetting of single deformed cavitation bubbles near boundaries, J. Hydrodynam. **35**, 832 (2023).
[25] G.-H. Wang, Y. Du, Z.-J. Xiao, J. Huang, Z.-Y. Wang, H.-C. Li, J.-Z. Wang, and Y.-W. Wang, Numerical study on formation of a splash sheet induced by an oscillating bubble in extreme vicinity to a water surface, J. Hydrodynam. **34**, 1021 (2023).

[26] E. A. Brujan, G. S. Keen, A. Vogel, and J. R. Blake, The final stage of the collapse of a cavitation bubble close to a rigid boundary, Phys. Fluids **14**, 85 (2002).
[27] M. Saini, E. Tanne, M. Arrigoni, S. Zaleski, and D. Fuster, On the dynamics of a collapsing bubble in contact with a rigid wall, J. Fluid Mech. **948**, A45 (2022).
[28] A. B. Sieber, D. B. Preso, and M. Farhat, Dynamics of cavitation bubbles near granular boundaries, J. Fluid Mech. **947**, A39 (2022).
[29] J. L. Huang, J. Z. Wang, J. Huang, P. Y. Lv, H. Y. Li, and Y. W. Wang, Effects of wall wettability on vortex flows induced by collapses of cavitation bubbles: A numerical study, Phys. Fluids **35**, 087122 (2023).
[30] E. A. Brujan, T. Noda, A. Ishigami, T. Ogasawara, and H. Takahira, Dynamics of laser-induced cavitation bubbles near two perpendicular rigid walls, J. Fluid Mech. **841**, 28 (2018).
[31] Q. Y. Zeng, S. R. Gonzalez-Avila, and C. D. Ohl, Splitting and jetting of cavitation bubbles in thin gaps, J. Fluid Mech. **896**, A28 (2020).
[32] D. Lohse, Fundamental fluid dynamics challenges in inkjet printing, Annu. Rev. Fluid Mech. **54**, 349 (2022).
[33] P. Gregorcic, R. Petkovsek, and J. Mozina, Investigation of a cavitation bubble between a rigid boundary and a free surface, J. Appl. Phys. **102**, 094904 (2007).
[34] A. M. Zhang, P. Cui, and Y. Wang, Experiments on bubble dynamics between a free surface and a rigid wall, Exp. Fluids **54**, 1602 (2013).
[35] G. H. Huang, M. D. Zhang, X. J. Ma, Q. Chang, C. Zheng, and B. Huang, Dynamic behavior of a single bubble between the free surface and rigid wall, Ultrason. Sonochem. **67**, 105147 (2020).
[36] L. T. Liu, J. X. Wang, Y. F. Zhang, K. Tang, and T. Ma, Coupling characteristics between bubble and free surface in a shallow water environment, Ocean Eng. **237**, 109577 (2021).
[37] P. Cui, A. M. Zhang, S. P. Wang, and Y. L. Liu, Experimental study on interaction, shock wave emission and ice breaking of two collapsing bubbles, J. Fluid Mech. **897**, A25 (2020).
[38] R. Han, A. M. Zhang, S. C. Tan, and S. Li, Interaction of cavitation bubbles with the interface of two immiscible fluids on multiple time scales, J. Fluid Mech. **932**, A8 (2021).
[39] A. Zelinsky, Learning opencv—Computer vision with the opencv library (G. R. Bradski *et al.*, 2008), IEEE Robot. Autom. Mag. **16**, 100 (2009).
[40] J. P. Best, The Dynamics of Underwater Explosions, Ph.D. thesis, University of Wollongong, 1991.
[41] J. P. Best, The formation of toroidal bubbles upon the collapse of transient cavities, J. Fluid Mech. **251**, 79 (1993).
[42] J. R. Blake, D. M. Leppinen, and Q. X. Wang, Cavitation and bubble dynamics: The kelvin impulse and its applications, Interface Focus **5**, 20150017 (2015).
[43] Y. A. Ilinskii, M. F. Hamilton, and E. A. Zabolotskaya, Bubble interaction dynamics in lagrangian and hamiltonian mechanics, J. Acoust. Soc. Am. **121**, 786 (2007).
[44] W. Lauterborn and C. D. Ohl, Cavitation bubble dynamics, Ultrason. Sonochem. **4**, 65 (1997).
[45] P. Koukouvinis, G. Strotos, Q. Y. Zeng, S. R. Gonzalez-Avila, A. Theodorakakos, M. Gavaises, and C. D. Ohl, Parametric investigations of the induced shear stress by a laser-generated bubble, Langmuir **34**, 6428 (2018).
[46] J. M. Rosselló, H. Reese, and C. D. Ohl, Dynamics of pulsed laser-induced cavities on a liquid-gas interface: From a conical splash to a 'bullet' jet, J. Fluid Mech. **939**, A35 (2022).
[47] M. Koch, C. Lechner, F. Reuter, K. Kohler, R. Mettin, and W. Lauterborn, Numerical modeling of laser generated cavitation bubbles with the finite volume and volume of fluid method, using openfoam, Comput. Fluids **126**, 71 (2016).
[48] See Supplemental Material at http://link.aps.org/supplemental/10.1103/PhysRevFluids.9.053602 for video of formation of a free vortex at $\gamma_r = 1$ and $\gamma_w = 2$; for video of formation of a wall vortex at $\gamma_r = 1$ and $\gamma_w = 1$.